A General Mechanism for the General Stress Response in Bacteria

Rishika Baral[1,2], Kristin Ho[1], Prem K. Ramasamy[1], Jesse B. Hopkins[3], Maxwell B. Watkins[4], Salvatore LaRussa[1,2], Suhaily Caban-Penix[1,5], Logan A. Calderone[1,2], and Niels Bradshaw[1*]

[1]Department of Biochemistry, Brandeis University, Waltham, Massachusetts, USA

[2]Graduate program in Biochemistry and Biophysics, Brandeis University, Waltham, Massachusetts, USA

[3]Biophysics Collaborative Access Team (BioCAT), Department of Physics, Illinois Institute of Technology, Chicago, Illinois, USA

[4]Biophysics Collaborative Access Team (BioCAT), Department of Biology, Illinois Institute of Technology, Chicago, Illinois, USA

[5]Graduate program in Molecular and Cell Biology, Brandeis University, Waltham, Massachusetts, USA

[*]To whom correspondence should be addressed: niels@brandeis.edu

Abstract

Bacteria have a widely conserved General Stress Response (GSR) that allows them to survive adverse environmental conditions. However, because the signaling proteins that initiate the GSR have evolved to respond to a vast range of species-specific signals, we lack a general understanding of how they are controlled. Here, we determined the molecular mechanism by which a member of the PPM family of protein serine/threonine phosphatases, RsbU, activates the GSR in *B. subtilis*. It was known that the phosphatase activity of RsbU is activated through interaction with a partner protein, RsbT, when it is released from a megadalton stress-sensing

complex upon environmental stress, but how RsbT activates RsbU was not understood. Here we report that RsbT binds an otherwise flexible linker of RsbU to dimerize and activate its phosphatase domains through a conserved allosteric switch element. Conformational flexibility of the homologous linker was known to control activity of the *E. coli* GSR-activating protein (RssB), which lacks phosphatase activity and functions as a protease adapter protein, suggesting a unifying model for GSR activation across bacterial phyla. Furthermore, and as we now show, the crossing α-helical conformation of RsbU linkers in the active dimeric state is similar to that predicted for paralogous bacterial phosphatases with diverse N-terminal sensory domains, and to linkers known to control the activity of GGDEF diguanylate cyclases and histidine kinases. We propose that this shared regulatory mechanism provides a modularly exchangeable toolkit for bacteria to recognize diverse environmental signals.

Introduction

The General Stress Response (GSR) allows bacteria to survive in hostile and changing environments[1-5]. A defining feature of the GSR is that it controls transcription of a large and diverse set of genes, dramatically reshaping the physiology of the organism (Gottesman 2019; Guerreiro et al. 2020; Boekhoud et al. 2020; Boylan et al. 1993). Another defining feature is that the GSR is induced by a variety of stress conditions that are frequently associated with each other, including stationary phase, nutrient depletion, cellular damage, and (for pathogens) host defense mechanisms (Gottesman 2019). This multiplicity of initiating conditions allows cells to anticipate and prepare for accumulating adversity, suggesting why the GSR is present in every bacterial species that has so far been analyzed. The GSR additionally contributes to pathogenesis through expression of genes controlling virulence, biofilm formation, and quorum sensing (Kint

et al. 2017; Battesti et al. 2011; Bartolini et al. 2019). Inactivation of the GSR, in turn, promotes the transition to long-term slow growth and antibiotic resistance, which are particularly important for persistent infections (Tuchscherr & Löffler 2016; Herbert et al. 2010; Bergkessel et al. 2016). Thus, deciphering the mechanisms that govern GSR activity is critical to understanding how bacteria interact with and adapt to their environments.

A major barrier to understanding initiation of the GSR is that we lack a unique, generalizable mechanistic model for how the activating signaling proteins have evolved to respond to species-specific signals. In a widespread mechanism for initiating the GSR, a member of the PPM family of serine/threonine phosphatases dephosphorylates a phosphorylated substrate protein to activate an alternative σ-factor through a "partner-switching" mechanism (Hecker et al. 2007), but how the phosphatase receives and is activated by an upstream signal has not been determined.

In this study, we address how the GSR phosphatase RsbU from *B. subtilis* is regulated (Yang et al. 1996) and present evidence that this mechanism is widely conserved. RsbU dephosphorylates a single phospho-serine on its substrate protein (RsbV) to release the GSR transcription factor (σ^B) from inhibition by an anti-sigma factor (RsbW) (Fig. 1A). RsbU has an N-terminal four-helix bundle dimerization domain that is also the binding site for RsbT, which activates RsbU as a phosphatase (Fig. 1C,D) (Delumeau et al. 2004). RsbT is sequestered in a megadalton stress sensing complex called the stressosome, and is released to bind RsbU in response to specific stress signals (Marles-Wright et al. 2008). We and others have reconstituted RsbU activation by RsbT (Delumeau et al. 2004; Ho & Bradshaw 2021), but how RsbT activates RsbU was not known.

This “partner-switching” mechanism is broadly conserved, and the activating phosphatases are observed to have diverse N-terminal sensory domains including PAS (Vijay et al. 2000; Greenstein et al. 2009; Fernández Martínez et al. 2009), response-receiver (de Been et al. 2010; Rodríguez-Martínez et al. 2023), GAF (Kint et al. 2019), and HAMP (Mittenhuber 2002). These signaling domains are frequently found as N-terminal regulators of histidine kinases and GGDEF diguanylate cyclases in bacteria, but whether or not there are shared mechanistic features between the regulatory principles of PPM phosphatases and these other signaling effector families is not known (Möglich et al. 2009; Galperin 2006).

We previously described a mechanism for allosteric control of the related *B. subtilis* phosphatase SpoIIE, which regulates endospore formation through a partner-switching mechanism analogous to RsbU control of the GSR (Ho & Bradshaw 2021; Bradshaw et al. 2017). Two helices of the PPM domain (α1 and α2), which we refer to as the switch element, change conformation to recruit metal cofactor and activate SpoIIE (Bradshaw et al. 2017). Based on analysis of structural and genetic data, we conjectured that this conformational change exemplifies a common mechanism among diverse phosphatases. However, we could not propose a specific model for how unrelated regulatory domains modularly control the switch conformation. For RsbU, we found that RsbT enhances phosphatase activity by increasing the efficacy of metal cofactor binding and that substitution of an amino acid in α1 ($RsbU^{M166V/L}$) activates RsbU in the absence of RsbT (Ho & Bradshaw 2021) These results supported our proposal that the switch element controls RsbU activation, but they did not reveal how RsbT binding to the N-terminus of RsbU is transduced to the switch.

One broadly conserved feature of GSR phosphatases (absent in SpoIIE) is an α-helical linker of variable length, which is N-terminal to the PPM phosphatase domain. Genetic data suggest that this linker regulates a paralogous *B. subtilis* GSR phosphatase (RsbP) (Brody et al. 2009). Here we report that binding of RsbT to the N-terminus of RsbU rigidifies an otherwise flexible linker to dimerize the C-terminal phosphatase domains through an interface mediated by the switch element. Importantly, and as we now report, this mechanism is generalizable to other PPM phosphatases and reveals a widespread feature of bacterial signaling.

Results

The linker controls RsbU activation through a predicted phosphatase dimer

We previously conducted a genetic screen (Ho & Bradshaw 2021) to identify variants of RsbU that are active in the absence of RsbT. Focusing on the phosphatase domain in our initial study, we reported identification of an amino acid substitution in α1 ($RsbU^{M166V/L}$) that links the switch element to RsbU activation (Ho & Bradshaw 2021). From this screen, we isolated a second variant, $RsbU^{Q94L}$, located in the linker of RsbU between the N-terminal dimerization domain and the C-terminal phosphatase domain (Fig. 1B-D). *rsbU*^{Q94L} strains activated σ^B in the absence of *rsbT*. This activation is comparable to when *rsbT* is overexpressed to exceed the capacity of the stressosome and is stronger than what we observe in strains expressing *rsbU*$^{M166V/L}$ (Fig. 1B).

To visualize how the Q94L and M166V/L substitutions could impact RsbU structure and activity, we generated an AlphaFold2 model of an RsbU dimer (Jumper et al. 2021; Mirdita et al.

2022) (Fig. 1D). The N-terminal region of RsbU is known to form a dimer, and RsbU is dimeric in our purifications (Fig. S1A) (Delumeau et al. 2004). In our model, the linkers form extended alpha-helices (82-112) that cross to connect dimers of the RsbU N-terminal domains and C-terminal phosphatase domains, with Q94 buried in the linker interface and M166 buried in the core of the phosphatase domain (Fig. 1D).

The crossing linker helices have similar conformation to homologous linkers observed in crystal structures of *P. aeruginosa* RssB, a phosphatase/adapter protein that also controls the GSR (PDB 3F7A and 3EQ2). RssB has an N-terminal response-receiver domain in place of the RsbU four helix bundle dimerization domain, suggesting that linker conformation is a conserved feature of PPM phosphatase dimers with divergent N-terminal regulatory domains (Fig. S2C). The linker helices in the RsbU prediction and the RssB structure splay apart as they enter the PPM domain with similar angle (pitch angles (α) based on Crick parameters for coiled-coils –17.6º and –18.4º respectively) and pack against α-1 of the PPM fold (Grigoryan & DeGrado 2011). Interestingly, we observed that other bacterial signaling proteins that are regulated by coiled-coil linkers had similar pitch angle for the helices connecting to the catalytic domains (for example the dimeric histidine kinase CheA, 1B3Q, α –16.8º, and the dimeric GGDEF diguanylate cyclase PadC, 5LLW, α –14.3º) (Bilwes et al. 1999; Gourinchas et al. 2017; Grigoryan & DeGrado 2011) (Fig S2C). Thus, the linker of RsbU could be a conserved regulatory feature, analogous to linkers of histidine kinases and GGDEF diguanylate cyclases.

Analysis of the RsbU dimer model using Socket2 identifies amino acids 83-97 as a two-turn coiled coil, with Q94 unfavorably packing against leucine 90 (Kumar & Woolfson 2021) (Fig.

S2A). To test whether hydrophobicity at position 94 promotes an active state, we tested the activity of RsbU alleles with different amino acid substitutions at position 94 for σ^B in wildtype and *rsbT* deleted strains. We found that substitutions of Q94 with amino acids that could pack at the intersection of the crossing linker helices (hydrophobic residues isoleucine, valine, and methionine, as well as tyrosine) resulted in mild constitutive, RsbT independent activation of σ^B that was further heightened by RsbT (Fig. S2B). Aromatic hydrophobic residues (phenylalanine and tryptophan) drove constitutive, RsbT dependent activation of RsbU (Fig. S2B). Substitutions of small or charged residues (alanine, glycine, glutamate, and asparagine) did not lead to activity in either strain (Fig. S2B). These results are consistent with a model in which burial of the amino acid at position 94, such as in the crossed helices of our prediction for RsbU dimer structure, drives RsbU activation.

RsbT binding to RsbU is influenced by the linker

One prediction of our hypothesis that RsbT stabilizes the crossed alpha helices of the RsbU dimer, is that RsbT should bind more tightly to $RsbU^{Q94L}$ than to RsbU. To test this, we measured the binding affinity of RsbT for RsbU using fluorescence anisotropy. From these data we obtained a K_D of 4.5 ± 1 μM, which decreased approximately 10-fold for $RsbU^{Q94L}$ (0.56 ± 0.2 μM) (Fig. 2A). Thus, $RsbU^{Q94L}$ stimulates RsbU phosphatase activity by an on-pathway mechanism, supporting the idea that RsbT binding stabilizes the linker in a dimerized conformation to activate RsbU.

RsbU phosphatase activation is controlled by the linker

We previously found that RsbT activates RsbU by simultaneously decreasing the K_M for manganese cofactor and increasing the k_{cat} for dephosphorylation of RsbV-P (Ho & Bradshaw 2021). To test whether RsbU Q94L substitution works by the same kinetic mechanism, we measured dephosphorylation of ^{32}P-phosphorylated RsbV by RsbU^{Q94L} (Fig. 2B). The k_{cat} of RsbU^{Q94L} was nearly the same as for the basal activity of RsbU (2.4 ± 0.1 min^{-1} compared to 1.4 ± 0.1 min^{-1}, and stimulated more than ten-fold by RsbT, 15 ± 0.4 min^{-1}) (Fig. 2B) (Ho & Bradshaw 2021). However, RsbU^{Q94L} had a K_M for $MnCl_2$ (1.4 ± 0.2 mM) that is more than fifty-fold reduced compared to RsbU alone (77 ± 9 mM) (Ho & Bradshaw 2021), and similar to the K_M^{MgCl2} of RsbU in the presence of RsbT (0.98 ± 0.07 mM (Ho & Bradshaw 2021)) (Fig. 2B). Addition of RsbT did not change the K_M of RsbU^{Q94L} for $MnCl_2$ (1.9 ± 0.6 mM), but the maximum catalytic rate of dephosphorylation increased nearly four-fold to 9.0 ± 0.64 min^{-1}, approaching the rate of RsbU stimulated by RsbT (Fig. 2B). Thus, RsbU^{Q94L} substantially recapitulates RsbT activation by decreasing the K_M for Mn^{2+}.

Because magnesium is more abundant in the cell than manganese, we considered that it may be the physiologically relevant divalent metal cofactor for RsbU and therefore determined whether the effects of RsbT and Q94L substitution depend on the metal cofactor used (Fig. 2C). Consistent with our observations with manganese, RsbT increased the k_{cat} of RsbU (from 0.09 ± 0.02 min^{-1} to 2.2 ± 0.2 min^{-1}) and decreased the K_M for $MgCl_2$ (from 85 ± 40 mM to 11 ± 3 mM). Three notable differences are that the basal k_{cat} is lower with magnesium, the K_M for $MgCl_2$ is higher, and the magnitude of the effect of RsbT is reduced (Fig. 2C). Together, these changes balance the effect of higher cellular concentration of magnesium and suggest that either metal may be physiologically relevant.

In contrast to our observations with manganese, we observed that $RsbU^{Q94L}$ increases k_{cat} nearly a hundred-fold (7 ± 1 min^{-1}) but does not change K_M for magnesium (52 ± 14 mM) (Fig. 2C). RsbT had additional modest effects on the k_{cat} (13 ± 1 min^{-1}) and the K_M for magnesium (38 ± 8 mM) of $RsbU^{Q94L}$ (Fig. 2C). Together, these data demonstrate that $RsbU^{Q94L}$ is an on-pathway variant that kinetically resembles RsbU activated by RsbT, but the identity of the metal cofactor determines the step in the reaction that is most strongly affected (metal binding or catalysis). This is consistent with previous findings that the allosteric switch controlling phosphatase activity of SpoIIE couples cofactor interaction and catalysis. Additionally, these results demonstrate that the linker transduces RsbT binding to control the active site of RsbU.

RsbT binds to the linker and N-terminal domain

To visualize how RsbT could control the linker to activate RsbU, we generated an AlphaFold2 prediction of a heterotetrameric complex between RsbT and RsbU (Fig. 3A). In this model, RsbU adopts a conformation very similar to our prediction of the RsbU dimer (RMSD 1.36 Å), suggesting that our AlphaFold2 RsbU dimer model represents the active state of RsbU even when RsbT was not included in the prediction. The predicted structure places RsbT in a hybrid interface that spans the N-terminal dimerization domain of both RsbU monomers and the linker of one monomer (Fig. 3A). Supporting the validity of the AlphaFold2 2RsbT/2RsbU model, residues previously implicated in RsbT/U binding (Hardwick et al. 2007) (Y28 and E24 from one RsbU monomer, I74, and I78 from the other RsbU monomer, and RsbT R19, R23, and N24) are all buried in the predicted interface (Fig. S3A).

To gain further insight into how RsbT binding is transduced to RsbU linker conformation and phosphatase activity, we performed a genetic screen to isolate suppressors of RsbU^{Y28I}, which was previously observed to abolish binding to RsbT (Hardwick et al. 2007). After screening a library of PCR mutagenized *rsbU*^{Y28I} and *rsbT*, we identified 11 variants that introduced substitutions to RsbU that suppress *rsbU*^{Y28I}: S49G, K53E, T89A, G92E, G92R, Q94L, T110S, V142A, K143E, C165Y, and M173I (Fig. 3A-B). We additionally isolated revertants that restored Y28 suggesting that the screen was near saturation, but did not isolate any suppressors in *rsbT*, which was also mutagenized. Mapping the RsbU^{Y28I} suppressor mutations onto our 2RsbU/2RsbT model suggests that they fall into three classes:

1. A first class of substitutions may restore the RsbT binding to the N-terminal dimerization domain of RsbU (revertants, S49G and K53E). S49 and K53 are predicted to be in close proximity to sidechains from the loop between the first and second α-helices of RsbT. Removing the sidechain of S49 and changing the charge of K53 may allow accommodation of RsbT in the presence of the Y28I substitution.
2. A second class of substitutions may promote linker dimerization and/or RsbT binding (T89A, G92E/R, and Q94L). T89 and G92 are positioned on the RsbU linker near Q94 and the predicted interface with RsbT. This proximity suggests that they could enhance RsbT interaction by promoting dimerization of the linker helices (similar to Q94L) and/or influencing the binding interactions between RsbT and the linker. Additionally, *rsbU*^{T89A} hyperactivates σ^B in a *ctc-lacZ* reporter strain when *rsbT* is present on the chromosome, consistent with these proposed mechanisms (Fig. S3B).

3. A third class of substitutions cluster around the regulatory switch of the RsbU phosphatase domain (helices α1 and α2 of the PPM fold, T110S, V142A, K143E, C165Y, and M173I). We hypothesize that these substitutions rescue RsbU^{Y28I} inactivation by promoting a constitutively active conformation of the RsbU phosphatase domain. Consistent with this, *rsbU*^{C165Y} caused σ^{B} activation in the absence of stress (Fig. S3B). The substituted amino acids are in three structural elements: switch helix α1, β2 and β3, which sit just above α1, and at the C-terminus of the linker helix (also referred to as α0), which is predicted to contact α1 of the same protomer and α1 and α2 across the dimer interface.

Contacts between RsbT and the RsbU linker drive phosphatase activation

To test the model that RsbT activates RsbU by directly interacting with the linker to dimerize the RsbU phosphatase domains, we introduced a substitution that would block this interaction (a charge swap at position R91, RsbU^{R91E}) and assayed RsbU activation (Fig. 3C). RsbU^{R91E} abolished σ^{B} activity for cells overexpressing *rsbT* (Fig. 3C), and in biochemical assays RsbT stimulation of RsbU^{R91E} phosphatase activity was abolished (Fig 3D). Finally, we introduced a potentially compensatory charge switch at position D92 of RsbT (RsbT^{D92K}) (Fig. 3C). Expression of *rsbT*^{D92K} partially restored σ^{B} activity to *rsbU*^{R91E} expressing cells, consistent with direct interaction between these residues (Fig. 3C). Together, these results suggest that contacts between RsbT and the linker of RsbU are responsible for phosphatase activation.

The RsbU linker is flexible in the absence of RsbT

We considered two models for why RsbU is inactive in the absence of RsbT. One possibility is that inactive RsbU resembles the dimeric structure predicted by AlphaFold2 and that RsbT

induces a subtle conformational change, for example changing the registry or pitch of the crossing linker helices. A second possibility is that the linkers of inactive RsbU are flexible and that the phosphatase domains only interact with each other when RsbT orders the linkers into a crossing conformation. To distinguish between these two models, we performed small angle X-ray scattering coupled to size exclusion chromatography with multi-angle light scattering (SEC-MALS-SAXS) to assess the shape and flexibility of RsbU dimers in solution (Table 1 and Fig. S4A). RsbU eluted as a single peak from the size exclusion column with an average molecular weight of 77 kDa (calculated dimeric molecular weight 77.3 kDa) determined by multi-angle light scattering (MALS) (Fig. S1A). However, our sample had a minor contaminant of heterodimeric complexes of RsbU in which one monomer is C-terminally truncated that could influence the SAXS analysis (Fig. S1B). We therefore deconvoluted the SAXS profiles using evolving factor analysis (EFA) in RAW to isolate scattering profiles from the individual components (Hopkins et al. 2017; Meisburger et al. 2016) (Fig. S4A-C).The EFA deconvolution identified a major component (MW 75.6 kDa calculated from V_c method), which eluted earlier than a smaller component (MW 48.8 kDa calculated from V_c method) (Table 1 Guinier fits, and Fig. S4A-C). We conclude that the larger component is an RsbU dimer, while the smaller fragment is likely a heterodimeric complex of RsbU and the C-terminal truncation product of RsbU (Fig. S1B).

We assessed the SAXS data for the RsbU dimer for features that report on flexibility (Kikhney & Svergun 2015). First, we compared the scattering intensity profile (I(q) vs. q) to a profile calculated from the AlphaFold2 model of an RsbU dimer using FoXS (Schneidman-Duhovny et al. 2016; Schneidman-Duhovny et al. 2013) The model was a poor fit to the data (χ^2 12.53), and

the data lacked distinct features caused by the multi-domain structure of RsbU from the AlphaFold2 model (Fig.4A). In contrast, multi-state modeling by MultiFoXS (Schneidman-Duhovny et al. 2016) which allows structural modeling of flexibility (we allowed flexibility for the linker residues 82-96 while keeping the N-terminal domain dimerized) produced a two-state solution with χ^2 of 1.2 (as compared to the one-state model with χ^2 of 1.58) and low residuals across the entire range of data (Fig. 4B). The structural models predicted by MultiFoXS depict a dimerized N-terminal domain with flexible linkers and PPM domains that do not make contact. The two conformations that were selected as the best fit to the scattering data by MultiFoXS also have very different R_g values, (34.91 Å (71%) and 45.69 Å (29%)), indicating RsbU samples a range of conformational space that includes a more compact state(s) consistent with the AlphaFold2 model and a significantly extended state(s) emphasizing that the linker is highly flexible. This can be visualized more readily from a dimensionless Kratky plot, which is bell-shaped and peaks above 1.3 (indicating that the RsbU dimer is non-globular) and lacks the two peaks from the FoXS computed model of the AlphaFold2 dimer structure that reflect the extended two domain structure of the prediction (Kikhney & Svergun 2015; Receveur-Bréchot & Durand 2012) (Fig. 4C, S4F). In contrast, the multi-state model predicted from MultiFoXS resembles the experimental data (Fig. 4C, S4F). The scattering data had several additional characteristic features indicating flexibility: the P(r) plot is smooth and has an extended tail (Cordeiro et al. 2017; Kikhney & Svergun 2015; Receveur-Bréchot & Durand 2012) (Fig. 4D), R_g and I(0) calculated from P(r) are larger than when calculated from Guinier fits (Cordeiro et al. 2017; Kikhney & Svergun 2015; Receveur-Bréchot & Durand 2012) (Table 1), molecular weight calculated using the MoW2 modified Porod volume method is an overestimate (Rambo & Tainer 2011) (Table 1), and the R_g (39.05 ± 0.16 Å) was larger than the R_g of the AlphaFold2 dimer

model (34.05 Å). Together, we conclude that the RsbU linker appears to be flexible in the absence of RsbT.

RsbT rigidifies and compacts the RsbU dimer

To test the hypothesis that RsbT rigidifies the linker to produce an active RsbU dimer, we attempted SEC-MALS-SAXS analysis of the RsbT/U complex. RsbT/U eluted with molecular weight (determined by MALS) of 88 kDa compared to 105 kDa for a 2RsbT/2RsbU heterotetramer (Fig. S1E), suggesting that the RsbT/U complex had largely disassembled on the column. We therefore performed SEC-MALS-SAXS on the RsbT/RsbU^{Q94L} complex, which has a higher affinity (Fig. S5A, S1C). The RsbT/U^{Q94L} complex eluted as a major peak with a higher molecular weight shoulder, with the average molecular weight of the main peak (determined by MALS) of 125 kDa (Fig. S1C). This is larger than the predicted molecular weight of a heterotetrameric 2RsbT/2RsbU^{Q94L} complex (105 kDa), suggesting that some higher order complexes form. EFA deconvolution (Meisburger et al. 2016) identifies a larger component that peaks at the leading edge of the main peak and has a R_g of 42.18 ± 0.48 Å, and a smaller component with R_g of 35.06 ± 0.43 Å and peak intensity within the main peak (Fig. S5B-D). We deduce that the smaller component represents that 2RsbT/2RsbU complex, supported by the molecular weight calculated from Porod analysis (103 kDa) and the position of the peak in the elution profile. Additionally, the R_g determined from Guinier fits (35.06 ± 0.43 Å) matches the R_g computed from the AlphaFold2 model of the heterotetrameric complex of 2RsbT/2RsbU using FoXS (33.68 Å) and is smaller than the R_g we observed for the RsbU dimer (39.05 ± 0.16 Å), indicating that the 2RsbT/2RsbU heterotetramer is a more rigid and compact complex. Fitting the scattering profile (I(q) vs. q) from this component to the AlphaFold2 model yielded a

χ^2 of 1.83, supporting the overall accuracy of the model (Fig. 4E). Multi-state modeling by MultiFoXS with the same flexibility parameters as the RsbU dimer produces a compact one-state model with a χ^2 of 1.96, which has a similar conformation to the AlphaFold2 prediction of 2RsbT/2RsbU heterotetramer (RMSD of 1.36Å) (Schneidman-Duhovny et al. 2016) (Fig. S5F). Additionally, the features of the scattering data that suggested flexibility for RsbU dimers all suggest that the RsbT/RsbU complex is more rigid (the quality of the FoXS fit, a lower peak of the dimensionless Kratky plot, and a shorter tail of the P(r) plot) (Cordeiro et al. 2017; Kikhney & Svergun 2015; Receveur-Bréchot & Durand 2012) (Fig. 4D-4F, S5G). The identity of the higher molecular weight component of the scattering data is ambiguous, but could represent a larger assembly of RsbT/RsbU^{Q94L} or multimers of RsbU^{Q94L} that were observed when RsbU^{Q94L} was analyzed alone (Fig. S1F). Together, these data support the validity of the AlphaFold2 model of the heterotetrameric 2RsbT/2RsbU complex, and additionally suggest that RsbT rigidifies the otherwise flexible linker of RsbU to dimerize the phosphatase domains.

RsbU is activated through a conserved switch element

The dimerized phosphatase domains of our RsbU model are positioned similarly as they are in the crystal structure of dimerized, active, SpoIIE and in the crystal structure of *P. aeruginosa* RssB (Bradshaw et al. 2017) (Fig. S1C, 5C). In our model, and these empirical examples, the interface between the phosphatase domains is mediated through helices α1 and α2, which were previously established as an allosteric regulatory element that couples metal cofactor binding, catalytic rate, and substrate recognition for SpoIIE and RsbU (Ho & Bradshaw 2021) (Fig. 1C-D). M166 is located in α1 and is predicted to be buried in the core of the phosphatase domain making contacts with β2 of the phosphatase domain and the C-terminal end of the linker helix

(Fig. 1C-D). Thus, the predicted structure suggests that RsbU activity is controlled by dimerization-dependent conformational change of α1 and α2 of the phosphatase domain. A prediction of this hypothesis is that $RsbU^{M166V}$, which we isolated as a RsbT independent RsbU variant (Ho & Bradshaw 2021), should activate RsbU by promoting recruitment of metal cofactor and increasing k_{cat}, similar to RsbT. We therefore measured the activity of $RsbU^{M166V}$ and found that the k_{cat} was increased eighty-fold (7.03 ± 0.35 min^{-1}) and the K_M for $MgCl_2$ was reduced four-fold (19.0 ± 2.1 mM) to levels comparable to RsbT stimulated values (Fig. S6). Thus, our results suggest that RsbT-induced rigidification of the RsbU linker activates RsbU as a phosphatase by dimerizing the phosphatase domains and inducing conformational change of a conserved switch element.

Regulated dimerization is an evolutionarily adaptable mechanism to control bacterial phosphatases

B. subtilis has a second GSR-initiating PPM phosphatase, RsbP, that has an N-terminal PAS domain and dephosphorylates RsbV to activate σ^B in response to energy stress. Our AlphaFold2 prediction of an RsbP dimer shows an extended alpha-helical linker connecting dimeric PAS domains and phosphatase domains. Like RsbU, the interface between the dimerized phosphatase domains is predicted to be mediated by α1 and α2 of the phosphatase domain. We found that previously identified constitutively activating mutations in RsbP (Brody et al. 2009) map to similar positions as the gain-of-function mutations we identified here for RsbU in their respective predicted structures, namely the interface between α1 and α2 of the phosphatase domains and the linker. RsbP is activated by a partner-protein, RsbQ, that has analogous function to RsbT for RsbU. An AlphaFold2 prediction of the heterotetrameric 2RsbP/2RsbQ complex

places the two molecules of RsbQ in a hybrid interface between the PAS domains and linkers, similar to how RsbT contacts RsbU, suggesting that key features of the activation mechanism are conserved (Fig. 5A).

To further probe the generality of the linker-mediated phosphatase dimer we observe for RsbU, we generated AlphaFold2 predictions for dimers of other documented GSR initiating phosphatases (*C. difficile* RsbZ (N-terminal tandem GAF domains) (Fig. 5B), *S. coelicolor* OsaC (N-terminal GAF and PAS domains), and *M. tuberculosis* Rv1364c (N-terminal PAS domain, C-terminally fused to an anti-σ factor domain and an anti-anti-σ factor domain)), as well as from examples of common domain architectures of PPM phosphatases selected from InterPro (response receiver (*Streptomyces coelicolor*, MY40396.1), GAF (*Rhodococcus aetherivorans*, WP_029544106.1), and HAMP (*Synechocystis sp.*, WP_010874143.1) domains) (Fig. S7). In each case AlphaFold2 produced high-confidence predictions of phosphatase domains dimerized through a shared α0, α1, α2 interface, connected to dimeric N-terminal domains by crossing α-helical linkers (Fig. S7-8). From this analysis, we conclude that linker-mediated phosphatase domain dimerization is likely an evolutionarily conserved, adaptable mechanism to control PPM phosphatase activity. This mechanistic/structural congruence provides a framework for how distantly related phosphatases can be regulated to control diverse biological processes in bacteria (Fig. 5E).

Discussion

Since the ground-breaking discovery of σ^B, the first conditionally-activated cellular transcription factor to be identified, forty-five years ago (Haldenwang & Losick 1979), a persistent

unanswered question has been how σ^B is turned on. Here, our findings reveal how RsbU is activated as a phosphatase in the decisive step of σ^B activation. Below, we describe how this mechanism is broadly applicable to other bacterial signaling pathways.

RsbT activates RsbU through a conserved phosphatase dimer

Using unbiased genetic screens, biochemical reconstitution, biophysical approaches, and structural prediction, we have discovered that RsbT activates RsbU by rigidifying an otherwise flexible linker region to allosterically activate RsbU as a phosphatase. Our structural prediction, supported by our genetic and structural data suggest that RsbU linkers assume a crossed α-helical conformation that dimerizes the phosphatase domains. This dimerization activates RsbU through a conserved switch element at the dimer interface, decreasing the K_M for metal cofactor and increasing the catalytic rate. Our structural predictions suggest that this is a widespread mechanism to regulate the activity of bacterial protein serine/threonine phosphatases.

A general mechanism for general stress response activation

E. coli and *B. subtilis* are the most extensively studied models for GSR activation (Battesti et al. 2011; Hecker et al. 2007). However, key mechanistic features of the activation mechanisms differ between the two systems. The *E. coli* GSR is initiated by stabilizing the alternative sigma factor σ^S (RpoS) against degradation by ClpXP (Fig. 5C). Under non-stressed conditions, degradation of σ^S is mediated by the adapter protein, RssB, which is inhibited by anti-adaptors (IraD, IraM, and IraP) and/or phosphorylation on its N-terminal response-receiver domain during stress. Historically, the differences between these systems were interpreted to mean that they operate by distinct mechanistic principles. However, RssB contains a C-terminally truncated

(and therefore inactive) PPM phosphatase domain, suggesting some aspects of its regulatory mechanism could be shared with RsbU(Battesti et al. 2013).

Our findings reveal that *E. coli* RssB and *B. subtilis* RsbU use three shared regulatory features to control GSR activation through their distinct downstream mechanisms. First, the positioning of analogous flexible linkers controls GSR activation by RssB and RsbU (Brugger, Schwartz, et al. 2023; Brugger, Srirangam, et al. 2023; Dorich et al. 2019). The C-terminal pseudo-phosphatase domain of RssB is joined to its N-terminal σ^S binding response-receiver domain by a predominantly α-helical linker (termed the segmented helical linker, or SHL) of similar length to the linker of RsbU (Dorich et al. 2019). The SHL folds to occlude the σ^S interacting face of the response-receiver domain when bound to anti-adapters or when the response-receiver domain is phosphorylated (Brugger, Schwartz, et al. 2023; Brugger, Srirangam, et al. 2023; Dorich et al. 2019). Supporting the hypothesis that the SHL is mechanistically related to the RsbU linker, substitution of W143, the homologous residue to Q94 of *B. subtilis* RsbU, blocks regulation by IraD and IraP (Battesti et al. 2013). Second, the interface between the linker and α1 of the phosphatase domain is critical for regulation of both RssB and RsbU (Brugger, Schwartz, et al. 2023; Dorich et al. 2019). W143 packs in a hydrophobic pocket formed with the α1 helix of the pseudo-phosphatase domain of phosphorylated RssB and IraD bound RssB (Brugger, Schwartz, et al. 2023; Dorich et al. 2019). Substitution of residues in α1, including A216 (corresponding to M166 of RsbU), block regulation of RssB by anti-adapters, underscoring the mechanistic similarity (Battesti et al. 2013). Third, conformational change of the switch helices (α1 and α2) of the phosphatase domain is of shared regulatory importance (Battesti et al. 2013). HDX experiments demonstrate that there is decreased exchange of the α1 helix of the pseudo-

phosphatase domain of RssB when σ^S is bound, suggesting that the conformational dynamics of this region are reduced by substrate recognition (Brugger, Schwartz, et al. 2023).

These striking mechanistic similarities between RssB from *E. coli* and RsbU from *B. subtilis* suggest that key regulatory features were conserved when an ancestral phosphatase lost enzymatic activity and became a dedicated adapter protein in *E. coli* and related γ-proteobacteria. Interestingly, *P. aeruginosa* has a homologue of RssB/RsbU that functions as an adapter for σ^S degradation, yet has a catalytically active, full length phosphatase domain and resides in an operon with an *rsbV* homologue (*rssC)* (Rodríguez-Martínez et al. 2023). Crystal structures of *P. aeruginosa* RssB revealed that it forms a dimer with crossing linkers and dimerized phosphatase domains with striking similarity to the dimer predicted for RsbU (Fig. 5C, S2C). Intriguingly, adapter protein function of *P. aeruginosa* RssB requires RssC (Rodríguez-Martínez et al. 2023), and *E. coli* RssB has been observed to weakly dimerize (Dorich et al. 2019), further supporting a direct mechanistic link between phosphatase regulation and adapter protein function. While not all GSR regulatory mechanisms involve a phosphatase or adapter protein related to RsbU/RssB, these findings suggest that linker-mediated control of a PPM phosphatase is a broadly conserved mechanism for GSR initiation across bacterial phyla.

An exchangeable toolkit for signal transduction

Histidine kinases and GGDEF diguanylate cyclases are the two most prevalent families of bacterial signal transduction proteins. A striking feature of their regulatory mechanisms is that they are often active in dimeric complexes that are allosterically controlled by N-terminal regulatory domains that propagate signals through crossing α-helical linkers (Zschiedrich et al.

2016; Randall et al. 2022; Gourinchas et al. 2017). Our finding that the crossing α-helical linkers are structurally similar (Fig. S2C) suggests that this shared allosteric regulatory architecture allows modular exchange of N-terminal domains between PPM phosphatases, histidine kinases, and GGDEF diguanylate cyclases. We predicted structures of dimeric PPM phosphatases with regulatory domains commonly associated with histidine kinases (response receiver and HAMP domains) and GGDEF diguanylate cyclases (PAS domains). In all cases, we observed conservation of a coiled-coil linker and of the α0/α1/α2 phosphatase domain dimer interface (Fig. 5, S7). Additionally, the RsbU N-terminal domain and RsbT were previously shown to control GGDEF diguanylate cyclase activity in *Moorella thermoacetica* (Quin et al. 2012), and histidine kinases with RsbU N-terminal domains are found in operons with *rsbT* and stressosome genes in some *Proteobacteria* species (Heinz et al. 2022) (Fig. 5D-E). The PAS/α/β hydrolase module that controls RsbP phosphatase activity in *B. subtilis* is similarly found coupled to histidine kinases and GGDEF diguanylate cyclases across bacterial phyla (Nadezhdin et al. 2011).

While the specific mechanism discovered here for linker control of RsbU activity (flexibility controlled by a binding partner) is distinct from the models for linker control of histidine kinases and GGDEF diguanylate cyclases (piston shift, scissoring, and helical rotation) (Zschiedrich et al. 2016; Randall et al. 2022), the shared dimeric architecture suggests that N-terminal regulatory domains could be modularly exchanged across effector domain families (Fig. 5F). Allosteric control of PPM switch element conformation could be achieved by piston shift, scissoring, or helical rotation. Future characterization of PPM phosphatases will be required to determine how

widespread linker flexibility is as a regulatory mechanism and how modularly sensory domains can be exchanged across signaling effector families.

Acknowledgements

The authors thank Richard Losick, Dorothee Kern, Chris Miller, Julia Kardon, Matthew Cabeen, Liz Hedstrom, Susan Lovett, Emily Stadnicki, and Maria-Eirini Pandelia for input at various stages of this project. Justin Curran, LuYing Pan, Spencer Clark, Alexis Ryan, and Wendy Yang additionally contributed to the research. This research used resources of the Advanced Photon Source, a U.S. Department of Energy (DOE) Office of Science User Facility operated for the DOE Office of Science by Argonne National Laboratory under Contract No. DE-AC02-06CH11357. BioCAT was supported by grant P30 GM138395 from the National Institute of General Medical Sciences of the National Institutes of Health. Use of the Pilatus 3 1M detector was provided by grant 1S10OD018090 from NIGMS. The content is solely the responsibility of the authors and does not necessarily reflect the official views of the National Institute of General Medical Sciences or the National Institutes of Health.

Author contributions

RB, conceptualization, investigation, data analysis, visualization, writing-original draft, writing-review and editing. KH, PR, conceptualization, data analysis, investigation. JH, investigation, data analysis, writing-review and editing. MW, SLR, SCP, LC, investigation. NB, conceptualization, visualization, writing-original draft, writing-review editing, and supervision.

Figure Legends:

Figure 1: The linker controls RsbU activation through a conserved switch element

A Reaction scheme of the RsbU dependent pathway of the environmental stress response. RsbU is activated by its partner protein RsbT (T, purple) to dephosphorylate its substrate protein RsbV-P (V-P). This displaces the GSR alternative sigma factor σ^B from inhibition by the anti-sigma factor RsbW (W) to initiate transcription of σ^B dependent genes (bold). **B** Amino acid substitutions in RsbU (Q94L and M166V) cause enhanced σ^B activity in *B. subtilis*. Strains carrying a lacZ reporter of σ^B activity (*ctc-lacZ*) were plated on X-gal indicator plates in the presence (top) or absence (bottom) of IPTG to induce expression of the *rsbU* constructs. Strains assayed either were deleted for *rsbT* at the chromosomal locus (–) or retained the chromosomal copy of *rsbT* (+). A control strain in which *rsbT* was additionally overexpressed on the plasmid with *rsbU* is indicated by oe. Plates were imaged after 24 hours of growth at 37ºC, which was shorter than the time used to visualize *lacZ* expression from the $rsbU^{M166V}$ strain previously (Ho & Bradshaw 2021). **C** Domain diagram of RsbU. The N-terminal domain of RsbU (blue) (amino acids 1-81) is joined to the α-helical linker domain (grey) (82-112), which connects it to the PPM phosphatase domain (grey) (121-335). The regulatory switch element of the PPM phosphatase domain is colored orange (156-201). The N-terminal domain contains the putative RsbT binding site and the catalytic and metal coordination site is contained in the phosphatase domain. The location of RsbT-bypass mutations are highlighted in green. **D** AlphaFold2 model of RsbU dimer. The N-terminal domains (blue), α-helical linkers (grey), and phosphatase domains (grey) are labeled, with the regulatory switch elements (α1 and α2) colored orange. The Cα atoms of residues Q94 and M166 are shown in green spheres.

Figure 2: RsbU linker influences RsbT binding and phosphatase activity

A Mean anisotropy of RsbT-TMR (200 nM) is plotted as a function of RsbU concentration. The curves are fits to a quadratic binding equation using non-linear curve fitting. Wild-type RsbU (black) has a K_D of 4.5 ± 0.96 µM and $RsbU^{Q94L}$ (green) has a K_D of 0.56 ± 0.15 µM. The lower plot is an inset of RsbU concentrations to 10 µM. Below is the reaction scheme of RsbT binding to RsbU with the values for the calculated K_D below. **B** The rate of dephosphorylation of RsbV-P is plotted as a function of concentration of $MnCl_2$. Observed rates for RsbU in the presence (black) and absence (grey) of RsbT and $RsbU^{Q94L}$ in the presence (green) and absence (light green) of RsbT are shown. Curves are fits to the Michaelis-Menten equation using non-linear curve fitting. The k_{cat} of wild-type RsbU is 15 ± 0.35 min^{-1} with RsbT and 1.4 ± 0.077 min^{-1} without RsbT and the k_{cat} of $RsbU^{Q94L}$ is 9.0 ± 0.64 min^{-1} with RsbT and 2.4 ± 0.084 min^{-1} without RsbT. The K_M^{MnCl2} of wild-type RsbU is 0.98 ± 0.069 mM with RsbT and 77 ± 9.0 mM without RsbT and the K_M^{MnCl2} of $RsbU^{Q94L}$ is 1.4 ± 0.19 mM with RsbT and 1.9 ± 0.56 mM without RsbT. The lower plot is an inset of wild-type RsbU in the absence of RsbT of $MnCl_2$ concentrations to 100 mM. Below is a summary of a reaction scheme of RsbU dephosphorylating RsbV-P (denoted as S) with Mn^{2+} cofactor, with the K_M^{MnCl2} and k_{cat} values below. Data for RsbU are reproduced from (Ho & Bradshaw 2021). **C** The rate of dephosphorylation of RsbV-P is plotted as a function of concentration of $MgCl_2$. Data and curve fits are colored as in **B**. Non-linear curve fits to the Michaelis-Menten equation gave k_{cat} of wild-type RsbU 2.2 ± 0.16 min^{-1} with RsbT and 0.088 ± 0.023 min^{-1} without RsbT and k_{cat} of $RsbU^{Q94L}$ 13 ± 1.1 min^{-1} with RsbT and 7.3 ± 1.2 min^{-1} without RsbT. The K_M^{MgCl2} of wild-type RsbU is 11 ± 2.6 mM with RsbT and 85 ± 38 mM without RsbT, and the K_M^{MgCl2} $RsbU^{Q94L}$ is 38 ± 8.4 mM with RsbT and 52 ± 14 mM without RsbT. The lower plot is an inset of wild-type

RsbU in the absence of RsbT. Below is a summary of a reaction scheme of RsbU dephosphorylating RsbV-P (denoted as S) with Mg^{2+} cofactor, with the K_M^{MgCl2} and k_{cat} calculated values below.

Figure 3: RsbT has a hybrid interface with RsbU N-terminal dimerization domain and linker

A An AlphaFold2 model of a heterotetrameric 2RsbT/2RsbU complex is shown in ribbon representation. RsbT (purple) binds with an interface that spans the N-terminal domains (blue) and α-helical linkers (grey) of both RsbU protomers. The PPM phosphatase domains are colored grey and the regulatory switch elements (α1 and α2) are colored orange. The Cα position of $RsbU^{Y28}$ is shown as a red sphere, and the Cα position of *rsbU*^{Y28I} suppressor substitutions are shown as green spheres. The Cα position of $RsbU^{R91}$ (dark) and $RsbT^{D92}$ (light) are shown as pink spheres. **B** Strains with a σ^B LacZ reporter were plated on IPTG/X-gal plates to induce expression of plasmid borne *rsbT* and *rsbU*^{Y28I} and visualize σ^B activity (indicated by blue pigmentation after 24 hours of growth at 37ºC). Additional amino acid substitutions in the *rsbU* gene are indicated above the spots, with the region where they are located in the RsbU structure specified. **C** Strains with a σ^B LacZ reporter were plated on IPTG/X-gal plates to induce expression of plasmid borne *rsbT* and *rsbU* with indicated changes to the RsbT and RsbU amino acid sequence. Plates were imaged after 36 hours of growth at 37ºC to allow the blue pigmentation from *rsbU*^{R91E}/*rsbT*^{D92K} expressing cells to be more visible. **D** R91E does not decrease the basal phosphatase activity of RsbU. Plots show dephosphorylation of RsbV-P (25 µM) by RsbU (black) and $RsbU^{R91E}$ (pink) (0.5µM) in the presence of 10 mM $MnCl_2$ and the presence or absence of 10 µM RsbT (lite colors) as a function of time. Linear fits of the data are

shown, with the slopes indicating the observed rates (k_{obs}). The k_{obs} for wild-type RsbU is 0.0206 ± 0.00124 min^{-1} without RsbT and 10.0 ± 0.628 min^{-1} with RsbT. The k_{obs} for $RsbU^{R91E}$ is 0.0379 ± 0.00543 min^{-1} without RsbT and 0.142 ± 0.0161 min^{-1} with RsbT. The lower plot is an inset of wild-type RsbU in the presence of RsbT to thirty minutes.

Figure 4: RsbU linker is flexible in the absence of RsbT, and is rigidified by RsbT binding. **A** I(q) versus q plot of the dimer component of SAXS scattering data from RsbU (blue) overlaid with a FoXS generated profile fit of the AlphaFold2 RsbU dimer structure (red). The upper plot shows I(q) versus q on log-linear axes while the lower plot shows the uncertainty normalized residuals of the fit ((experimental-computed)/error), χ^2 of 12.53. The AlphaFold2 model used for the fit is shown inset. **B** I(q) versus q plot of the dimer component of SAXS scattering data from RsbU (blue) overlaid with a MultiFoXS generated two-state profile fit with flexibility allowed for residues 82-96 (pink). The upper plot shows I(q) versus q on log-linear axes while the lower plot shows the uncertainty normalized residuals of the fit ((experimental-computed)/error), χ^2 of 1.2. The two best fit flexible models are shown with R_g and percentage of each model used in the fit indicated. **C** Dimensionless Kratky plot of SAXS scattering data from the dimer component of RsbU experimental data (blue). The experimental profile was logarithmically binned to reduce noise at high qR_g. **D** Normalized P(r) by I(0) versus r plot from SAXS scattering data from the dimer component of RsbU (blue) and heterotetrameric component of RsbT/$RsbU^{Q94L}$ complex (light blue). **E** I(q) versus q plot of the heterotetrameric component of SAXS scattering data from RsbT/$RsbU^{Q94L}$ complex (blue) overlaid with a FoXS generated profile fit of the AlphaFold2 RsbT/RsbU heterotetramer structure (red). The upper plot show I(q) versus q on a log-linear axes while the lower plot shows the uncertainty normalized residuals of the fits ((experimental-

computed)/error), χ^2 of 1.83. The RsbT/RsbU AlphaFold2 model used in the fit is shown as an inset. **F** Dimensionless Kratky plot of SAXS scattering data from the heterotetrameric component of RsbT/RsbU^{Q94L} complex experimental data (blue). The experimental profile was binned logarithmically to reduce noise at high qR_g values.

Figure 5: An exchangeable toolkit for bacterial signal transduction

A An AlphaFold2 model of the *B. subtilis* energy stress phosphatase RsbP is shown bound to its activating α/β-hydrolase protein RsbQ (purple) with a schematic of the σ^B activation pathway shown above. RsbP has an N-terminal PAS domain (turquoise) that is connected to the PPM phosphatase domain by a predicted coiled coil linker. The Cα positions of bypass suppressor mutations that render RsbP active in the absence of RsbQ(Brody et al. 2009) are shown as green spheres. The switch element of the PPM phosphatase domain (α1 and α2) is colored orange. **B** An AlphaFold2 model of the *C. difficile* GSR phosphatase RsbZ is shown with a schematic of the σ^B activation pathway shown above. RsbZ has tandem N-terminal GAF domains (blue) that connect to the PPM phosphatase domain by a predicted coiled coil linker. The switch element of the PPM phosphatase domain (α1 and α2) is colored orange. **C** Experimental structures of the GSR initiating adaptor protein RssB from *E. coli* (left, 8T85) and *P. aeruginosa* (right, 3F7A) are shown with a schematic of the σ^S activation pathway shown above. The Cα positions of a bypass suppressor mutation (W143R) that renders RssB insensitive to anti-adapter proteins is shown as a green sphere. The switch element of the PPM phosphatase domain (α1 and α2) is colored orange. **D** An AlphaFold2 model of a dimer of the histidine kinase NreB from a *Gammaproteobacteria* species (MBI3545564.1) is shown with the RsbU N-terminal domain colored blue and the histidine kinase domain colored pink. **E** An AlphaFold2 model of a dimer

of the GGDEF diguanylate cyclase MtG from *M. thermoacetica* (WP_011392981.1) is shown with RsbU N-terminal domain colored blue, GAF domain colored lite blue, and GGDEF domain colored green. **F** Schematic illustrating how various sensor domains (RsbU N-terminal dimerization domain, PAS, response receiver (RR), and GAF) can control various output activities (serine/threonine phosphatase (PPM), histidine kinase (HK), protease adaptor, and diguanylate cyclase (GGDEF). We hypothesize that the shared regulatory mechanism through a dimeric coiled-coil linker makes these regulatory domains modularly exchangeable across effector domains. Known mechanisms for how allosteric regulation is transmitted through the linker are listed.

Supplemental Figure 1: MALS estimate of molecular weight of RsbU dimer, RsbT/RsbU^{Q94L} complex, RsbT/RsbU complex, and RsbU^{Q94L}

A Plot of inline SEC-MALS analysis of RsbU with measured differential refractive index (blue, left axis) and the molecular weight calculated from MALS (red, right axis). **B** Denaturing SDS-PAGE gel of successive fractions from the equivalent range of the elution as shown in **A** from preparative size exclusion chromatography of the sample of RsbU used for SEC-MALS-SAXS. Black box denotes the C-terminal truncation product present in each lane of the main peak. **C** Plots from inline SEC-MALS analysis of RsbT/RsbU^{Q94L} complex with measured differential refractive index (blue, left axis) and the molecular weight calculated from MALS (red, right axis). **D** Denaturing SDS-PAGE gel of successive fractions from the equivalent range of the elution of RsbT/U^{Q94L} as shown in **C** from preparative size exclusion chromatography of the sample used for SEC-MALS-SAXS. Black box denotes lack of C-terminal truncation product during co-expression and purification of RsbT/RsbU^{Q94L} complex. * Denotes load samples on

gel. **E** Plots from inline SEC-MALS analysis of RsbT/U complex with measured differential refractive index (blue, left axis) and the molecular weight calculated from MALS (red, right axis). **F** Plot inline SEC-MALS analysis of $RsbU^{Q94L}$ with measured differential refractive index (blue, left axis) and the molecular weight calculated from MALS (red, right axis).

Supplemental Figure 2: Q94L stabilizes the packing interface of the coiled-coil of the linker

A Coil diagram of RsbU residues 83-97 generated using DrawCoil. Grey circles indicate non-polar residues, orange indicate polar residues, red indicate negatively charged residues, and blue indicate positively charged residues. The blue dashed line depicts a putative salt bridge. Residue Q94 (circled in green) sits in the interface of the coils and is shown packing with L90. **B** An allelic series of amino acid substitutions at position 94 of RsbU was generated in an *rsbU* expression plasmid. Plasmids were introduced into *B. subtilis* cells containing a LacZ reporter of σ^B activity that were deleted for *rsbT* (top) or with *rsbT* retained on the chromosome (bottom). Cells were plated on IPTG/X-gal plates to induce *rsbU* expression and to indicate σ^B activity (blue pigmentation). **C** α-helical pitch analysis of coiled-coil domains. The AlphaFold2 model of an RsbU dimer is overlayed with crystal structure of *P. aeruginosa* RssB (PDB 3F7A, purple, left). The helical linker region extending out of the coiled coil ($RsbU^{98-112}$) is shown (grey) overlaid with *T. maritima* transducing histidine kinase CheA (PDB 1B3Q, red, middle) and *Idiomarina* A28L diguanylyl cyclases PadC (PDB 5LLW, yellow, right). α angles from Crick parameterization analysis using CCCP are shown for the overlaid region.

Supplemental Figure 3: RsbT binds to the linker

A Interface of RsbT and N-terminal domain of RsbU. A ribbon representation is shown of the AlphaFold2 model of the heterotetrameric 2RsbT/2RsbU complex with RsbU N-terminal dimerization domain colored blue, the switch element of the PPM domain (α1 and α2) colored orange, and RsbT colored purple. The Cα of positions of amino acids implicated in the binding interface of RsbT and RsbU N-terminal dimerization domain(Hardwick et al. 2007) are represented on the AlphaFold2 structure as yellow spheres. **B** Strains with a σ^B LacZ reporter (*ctc-lacZ*) are shown plated on IPTG/X-gal plates to induce expression of *rsbU* with the indicated amino acid substitutions. *rsbU* was chromosomally deleted, but *rsbT* was retained at its native locus. σ^B activity is visualized by the blue pigment after 36 hours of growth at 37ºC.

Supplemental Figure 4: EFA deconvolution and Guinier analysis of RsbU dimer SAXS profiles

A SAXS data summary for RsbU. Series intensity (blue, left axis) versus frames, and R_g versus frame (red, right axis) are plotted. **B** The selected intensity range for EFA (black) (frame index 1330-1620), and the individual component ranges for deconvolution; blue denotes the range of frames where the scattering component we assigned as the c0, RsbU dimer, was detected (frame index 1330-1603) and orange denotes the range of frames where the scattering component that is c1, presumably from a RsbU heterodimer containing a c-terminal truncation product dimer (frame index 1357-1620). **C** Area normalized concentration profiles for the c0, RsbU dimer component (blue) and c1, RsbU heterodimer containing c-terminal truncation product dimer (orange). **D** Mean χ^2 values for the fit of the EFA deconvolution to the original scattering data. **E** Guinier fit for RsbU dimer component on the upper plot and uncertainty normalized residuals of the fit on the lower plot. The scattering data for the dimer component (red) is fit to the Guinier

approximation (blue). The blue dashed lines are the q_{min} and q_{max} at values 0.00356 $Å^{-1}$ and 0.0234 $Å^{-1}$, respectively. **F** Kratky plot of SAXS scattering data from the dimer component of RsbU experimental data (blue) overlaid with the profile computed by FoXS based on the AlphaFold2 model of an RsbU dimer (red) and the profile of the flexible model computed by MultiFoXS (pink). The experimental profile was logarithmically binned to reduce noise at high q.

Supplemental Figure 5: EFA deconvolution and Guinier analysis of RsbT/RsbU^{Q94L} SAXS profiles

A SAXS data summary for RsbT/RsbU^{Q94L}. Series intensity (blue, left axis) versus frames, and R_g versus frame (red, right axis) are plotted. **B** The selected intensity range for EFA (black) (frame index 1300-1540), and the individual component ranges for deconvolution; blue denotes the range of frames where the scattering component we assigned as c0, ambiguous component, was detected (1300-1461) and orange denotes the range of frames where the scattering component we assigned as c1, the 2RsbT/2RsbU^{Q94L} heterotetrametric complex, was detected (1318-1540). **C** Area normalized concentration profiles for 2RsbT/2RsbU^{Q94L} heterotetrameric complex (orange) and ambiguous component (blue). **D** Mean χ^2 values for the EFA deconvolution fit to the original scattering data. **E** Guinier fit for 2RsbT/2RsbU^{Q94L} heterotetrameric complex component on the upper plot and uncertainty normalized residuals of the fit on the lower plot. The scattering data for the dimer component (red) is fit to the Guinier approximation (blue). The blue dashed lines are the q_{min} and q_{max} at values 0.0033 $Å^{-1}$ and 0.0336 $Å^{-1}$, respectively. **F** I(q) versus q plot of the heterotetrameric complex component of SAXS scattering data from 2RsbT/2RsbU (blue) overlaid with a MultiFoXS generated two-state profile

fit with flexibility allowed for residues 82-96 (red). The upper plot shows I(q) versus q on log-linear axes while the lower plot shows the uncertainty normalized residuals of the fit ((experimental-computed)/error), χ^2 of 1.96. The one-state flexible model is shown with a RMSD to the AlphaFold2 prediction of 2RsbT/2RsbU of 1.36 Å. **G** Kratky plot of SAXS scattering data from the heterotetrameric component of 2RsbT/2RsbU experimental data (blue) overlaid with the profile computed by FoXS based on the AlphaFold2 model of an RsbT/RsbU heterotetramer (red). The experimental profile was logarithmically binned to reduce noise at high q.

Supplemental Figure 6: RsbU is activated through a conserved switch element

The rate of dephosphorylation of RsbV-P is plotted as a function of concentration of $MgCl_2$. The observed rates for $RsbU^{M166V}$ (green) and wild-type RsbU in the presence (black) and absence of RsbT (grey) are shown. The curves are fits to the Michaelis-Menten equation using non-linear curve fitting. The k_{cat} of wild-type RsbU is 2.2 ± 0.2 min^{-1} with RsbT and 0.09 ± 0.02 min^{-1} without RsbT, and the k_{cat} of $RsbU^{Q94L}$ is 7.0 ± 0.4 min^{-1} without RsbT. The K_M^{MgCl2} of wild-type RsbU is 11 ± 3 mM with RsbT and 85 ± 40 mM without RsbT, and the K_M^{MgCl2} of $RsbU^{M166V}$ is 19 ± 2 mM. The lower panel is a summary of a reaction scheme of RsbU dephosphorylating RsbV-P (denoted as S) with Mg^{2+} cofactor, with the K_M^{MgCl2} and k_{cat} calculated values below. Errors are the error of the fit.

Supplemental Figure 7: AlphaFold2 predictions of varying signaling PPM phosphatases

A An AlphaFold2 model of the *M. tubercolisis* GSR phosphatase Rv1364c is shown with a N-terminal PAS domain colored turquoise that connects to the PPM phosphatase domain colored grey, an anti-σ domain (related to RsbW) colored pink and an anti-anti-σ domain (related to

RsbV) colored purple. The switch element of the PPM phosphatase domain (α1 and α2) is colored orange. **B** An AlphaFold2 model of the *S. coelicolor* OsaC GSR phosphatase is shown with a N-terminal RsbW-like kinase domain colored in green, connected to a PAS domain colored in turquoise, tandem GAF domains colored in blue, and a PPM phosphatase colored in grey. The switch element of the PPM phosphatase domain (α1 and α2) is colored orange. **C** An AlphaFold2 model of a dimer of the phosphatase from *R. aetherivorans* (WP_029544106.1) is shown with the GAF domain colored in blue connected to the PPM phosphatase colored in grey. The switch element of the PPM phosphatase domain (α1 and α2) is colored orange. **D** An AlphaFold2 model of a dimer of the phosphatase from *S. coelicolor* (MYU40396.1) is shown with the response receiver domain colored in red connected to the PPM phosphatase colored in grey. The switch element of the PPM phosphatase domain (α1 and α2) is colored orange. **E** An AlphaFold2 model of a dimer of the phosphatase from *Synechocystis* species (WP_010874143.1) is shown with the HAMP domain colored in yellow connected to the PPM phosphatase colored in grey. The switch element of the PPM phosphatase domain (α1 and α2) is colored orange. The structure models in all panels are shown aligned by the top PPM domain to highlight the conservation of the PPM dimer in predictions of dimeric phosphatases with diverse regulatory domains.

Supplemental Figure 8: PAE plots of AlphaFold2 structure predictions

Predicted aligned error of the AlphaFold2 structure predictions of the following proteins: *B. subtilis* RsbU, *B. subtilis* 2RsbT (chains A, B)/2RsbU (chains C,D) complex, *B. subtilis* 2RsbP (chains A,B)/2RsbQ complex (chains C,D), *C. difficile* RsbZ, *Gammaproteobacteria* sp. NreB,

M. thermoacetica MtG, *M. tubercolisis* Rv1364c, *S. coelicolor* OsaC, *R. aetherivorans* WP_029544106.1, *S. coelicolor* MYU40396.1, and *Synechocystis* sp. WP_010874143.1.

Materials and Methods

Protein expression and purification

All proteins were expressed in *E. coli* BL21 (DE3) cells grown at 37ºC to an OD_{600} of 0.4 and induced at 16ºC for 14-18 hours with 1mM isopropyl β-d-1-thiogalactopyranoside (IPTG) unless otherwise specified. Cells were harvested and purified as follows:

RsbU and RsbU variants: Cell pellets were resuspended in lysis buffer with 1 mM phenylmethylsulfonyl fluoride (PMSF) (50 mM K•HEPES, pH 7.5, 100 mM NaCl, 20 mM imidazole, 10% glycerol, 0.5 mM dithiothreitol (DTT)), and were lysed using two passes in a microfluidizer at 10,000 PSI. Cell lysates were cleared by spinning at 16,000 RPM for 45 minutes in an Avanti JA-20 rotor. Cleared lysates were then run over a HisTrap HP column on an AKTA FPLC, washed with lysis buffer, and eluted with a gradient to 200 mM imidazole. RsbU was run on a Superdex200 16/600 column equilibrated with lysis buffer on an AKTA FPLC. Fractions were pooled and the 6-His tags were cleaved with 3C protease in dialysis to lysis buffer overnight at 4ºC. Cleaved tags and 3C protease were subtracted by passing over a column containing equilibrated Ni-NTA resin. 2 mM EDTA was added to cleaved protein prior to gel filtration run. RsbU was then further purified on a Superdex200 16/600 column equilibrated with 20 mM K•HEPES pH 7.5, 100 mM NaCl, 2 mM DTT on an AKTA FPLC. Fractions were pooled, concentrated to 200 µM, and flash-frozen and stored at -80ºC.

RsbT/U and RsbT/RsbU^{Q94L} co-expression: Cell pellets were resuspended in lysis buffer with 1 mM PMSF (50 mM K•HEPES pH 8.0, 200 mM NaCl, 20 mM imidazole, 10% glycerol, 0.5 mM DTT), and were lysed using two passes in a microfluidizer at 10,000 PSI. Cell lysates were cleared by spinning at 16,000 RPM for 45 minutes in an Avanti JA-20 rotor. Cleared lysates were then run over a HisTrap HP column on an AKTA FPLC, washed with lysis buffer, and eluted with a gradient to 200 mM imidazole. 2 mM EDTA was added to protein prior to gel filtration run. RsbT/RsbU was then further purified on a Superdex200 16/600 column equilibrated with 20 mM K•HEPES pH 8.0, 100 mM NaCl, 2 mM DTT on an AKTA FPLC. Fractions were pooled, concentrated to 200 µM, and flash-frozen and stored at -80ºC.

RsbT: Cells were resuspended in lysis buffer with 1 mM PMSF (50 mM K•HEPES pH 8.0, 100 mM NaCl, 20 mM imidazole, 10% glycerol, 2 mM $MgCl_2$, 0.1 mM ATP, 0.5 mM DTT), and were lysed using two passes in a microfluidizer at 10,000 PSI. Cell lysates were cleared by spinning at 16,000 RPM for 45 minutes in an Avanti JA-20 rotor. Cleared lysates were then run over 2 mL/L of cells of Ni-NTA resin slurry equilibrated with lysis buffer. The resin was then washed with 10 CV of lysis buffer. Ni-NTA resin was resuspended with 10 mL of lysis buffer with 400 mM imidazole, and was incubated for 10 minutes. RsbT was eluted off column, elution was tracked by Bradford Reagent. Additional elution buffer was added until all protein was eluted off column. The 6-His tags were cleaved with 3C protease in dialysis to lysis buffer overnight at 4ºC. Cleaved tags and 3C protease were subtracted by passing over a column containing equilibrated Ni-NTA resin. Protein was concentrated to approximately 50 uM, was flash-frozen and stored at -80ºC.

RsbV: RsbV was expressed in *E. coli* BL21 (DE3) cells grown at 37ºC to an OD_{600} of 0.4 and induced at 37ºC for 3-4 hours with 1mM IPTG. Cells were harvested and resuspended in lysis buffer with 1 mM PMSF (50 mM K•HEPES pH 8.0, 200 mM NaCl, 20 mM imidazole, 10% glycerol, 0.5 mM DTT), and were lysed using two passes on a microfluidizer at 10,000 PSI. Cell lysates were cleared by spinning at 16,000 RPM for 45 minutes in an Avanti JA-20 rotor. Cleared lysates were then run over a HisTrap HP column on an AKTA FPLC, washed with lysis buffer, and eluted with a gradient to 200 mM imidazole. 2 mM EDTA was added to protein prior to gel filtration run. The 6-His tags were cleaved with 3C protease in dialysis to lysis buffer overnight at 4ºC. Cleaved tags and 3C protease were subtracted by passing over a column containing equilibrated Ni-NTA resin. Cleaved protein was then further purified on a Superdex75 16/60 equilibrated in 20 mM K•HEPES pH 7.5, 150 mM NaCl, 10 % glycerol, 2 mM DTT. Fractions were pooled, concentrated to approximately 100 µM, and flash-frozen and stored at -80ºC.

RsbW: Cell pellets were resuspended in lysis buffer with 1 mM PMSF (20 mM K•HEPES pH 7.5, 200 mM NaCl, 20 mM imidazole, 10 mM $MgCl_2$, 10 % glycerol, and 0.5 mM DTT), and were lysed using two passes on a microfluidizer at 10,000 PSI. Cell lysates were cleared by spinning at 16,000 RPM for 45 minutes in an Avanti JA-20 rotor. Cleared lysates were then run over a HisTrap HP column on an AKTA FPLC, washed with lysis buffer, and eluted with a gradient to 200 mM imidazole. The 6H tag was left uncleaved to aid removal after phosphorylation reactions. RsbW was then further purified on a Superdex75 16/60 equilibrated

in 50 mM K•HEPES pH 7.5, 150 mM NaCl, 10% glycerol, and 2 mM DTT. Fractions were pooled, concentrated to approximately 100 µM, and flash-frozen and stored at -80ºC.

RsbV-P: RsbVW coexpression plasmid was expressed in *E. coli* BL21 (DE3) cells grown at 37ºC to an OD_{600} of 0.4 and induced at 37ºC for 3-4 hours with 1mM IPTG. Cells were harvested and resuspended in lysis buffer with 1 mM PMSF (50 mM K•HEPES pH 7.5, 50 mM KCl, 20 mM imidazole, 0.5 mM DTT), and were lysed using two passes on a microfluidizer at 10,000 PSI. Cell lysates were cleared by spinning at 16,000 RPM for 45 minutes in an Avanti JA-20 rotor. Cleared lysates were then run over a HisTrap HP column on an AKTA FPLC, washed with lysis buffer, and eluted with a gradient to 200 mM imidazole. The 6-His tags were cleaved with 3C protease in dialysis to lysis buffer overnight at 4ºC. Cleaved tags and 3C protease were subtracted by passing over a column containing equilibrated Ni-NTA resin. RsbVW was run on a Superdex75 16/60 column equilibrated with lysis buffer on an AKTA FPLC. Fractions of RsbVW coelution were pooled and RsbV was phosphorylated in dialysis at room temperature in lysis buffer with 5 mM ATP and 10 mM $MgCl_2$. RsbV-P Fractions were pooled, concentrated to 200 µM, and flash-frozen and stored at -80ºC. Dialyzed RsbVW were then concentrated and run on Superdex75 16/60 column equilibrated with 20 mM K•HEPES pH 7.5, 150 mM NaCl, 10% glycerol, 2 mM DTT. RsbV-P Fractions were pooled, concentrated to 200 µM, and flash-frozen and stored at -80ºC.

SEC-MALS-SAXS

Small Angle X-ray Scattering (SAXS) was performed at BioCAT (beamline 18ID at the Advanced Photon Source, Chicago) with in-line size exclusion chromatography (SEC) to

separate sample from aggregates and other contaminants and ensure optimal sample quality. In-line multiangle light scattering (MALS), dynamic light scattering (DLS) and differential refractive index (dRI) measurements were recorded for additional biophysical characterization (SEC-MALS-SAXS). The samples were loaded on a Superdex 200 10/300 Increase GL Column (Cytiva) run by a 1260 Infinity II HPLC (Agilent Technologies) at 0.6 ml/min. The flow passed in order through an Agilent UV detector, a MALS detector and a DLS detector (DAWN Helios II, Wyatt Technologies), and an RI detector (Optilab T-rEX, Wyatt) before the SAXS flow cell. The flow cell consists of a 1.0 mm ID quartz capillary with ~20 µm walls. A coflowing buffer sheath is used to separate sample from the capillary walls, helping prevent radiation damage (Kirby et al. 2016) . Scattering intensity was recorded using a Pilatus3 X 1M (Dectris) detector that was placed 3.682 m from the sample giving us access to a q-range of 0.0027 $Å^{-1}$ to 0.33 $Å^{-1}$. 0.5s exposures were acquired every 1 s during elution and data was reduced using BioXTAS RAW 2.1.4 (Hopkins et al. 2017) (Hopkins 2024). Buffer blanks were created by averaging regions flanking the elution peak and subtracted from all measured profiles. Because of the heterogeneity in the samples, evolving factor analysis (EFA) was used to deconvolve the scattering profiles of the overlapping components (Meisburger et al. 2016). These scattering profiles were used for subsequent analysis in RAW. The quality of the deconvolution was assessed based on the mean weighted χ^2 for each deconvoluted component and the χ^2 of the combined fit to each frame of the dataset (Fig. S4B-E; S5B-E). RAW was used to run GNOM from the ATSAS package (version 3.2.1) (Svergun 1992; Manalastas-Cantos et al. 2021). Description of each SAXS sample and results of the analysis are presented in Table 1 (Trewhella et al. 2017).The composition of each scattering component was determined based on the SAXS derived molecular weights, the MALS profile, and gels from the purification of the protein or

protein complex (Fig. S1; Table 1). Molecular weights and hydrodynamic radii were calculated from the MALS and DLS data respectively using the ASTRA 7 software (Wyatt). All samples were run in 20 mM HEPES pH 7.5, 100 mM NaCl, 5 mM DTT. Wild-type RsbU was run at a concentration of 3.5 mg/mL, RsbT/RsbU^{Q94L} was run at a concentration of 2.5 mg/mL, RsbU^{Q94L} was run at a concentration of 3.5 mg/mL, RsbT/RsbU was run at a concentration of 2.5 mg/mL. FoXS was used to calculated predicted scattering profiles from the model, and was compared to the experimental scattering profiles (Schneidman-Duhovny et al. 2016; Schneidman-Duhovny et al. 2013). Output parameters calculated using FoXS are provided in Table 1. MultiFoXS was used to generate a flexible structure ensemble with multicomponent fits and was compared to the experimental scattering profiles (Schneidman-Duhovny et al. 2016). MultiFoXS input and output parameters are provided in Table 1.

Fluorescence anisotropy

We site-specifically labeled RsbT with tetramethylrhodamine 5-maleimide (TMR) dye at its unique cysteine (position 6). We added increasing concentrations of RsbU and RsbU^{Q94L} to 200nM RsbT^{TMR} and measured the change in anisotropy (Fig. 2A). All measurements were done at 25ºC in 50 mM K•HEPES pH 7.5, 100 mM NaCl, and 10% glycerol. All measurements of spectra were conducted with a slit width of # nm, and anisotropy measurements were conducted with a slit width of # nm. The excitation wavelength was 551 nm and the emission wavelength was 577 nm. Anisotropy measurements were taken 30 seconds apart for 6 measurements, and then were averaged and plot against its corresponding concentration of RsbU. Anisotropy data was then fit to a quadratic binding curve using KaleidaGraph, reported errors are the error of the fit.

Phosphatase assays

Phosphatase assays were performed with RsbV-P that was labeled with ^{32}P by incubating RsbV (40 µM), 6His-RsbW (45 µM), and 100 µCi of γ-^{32}P ATP overnight at room temperature in 50 mM K•HEPES pH 7.5, 50 mM KCl, 10 mM $MgCl_2$, and 2 mM DTT. Unincorporated nucleotide was removed by buffer exchange using a Zeba spin column equilibrated in 50 mM K•HEPES pH 8.0, 100 mM NaCl. 6H-RsbW was then removed by Ni-NTA resin equilibrated in 50 mM K•HEPES pH 8.0, 100 mM NaCl, 20 mM imidazole. The flow-through fraction from the Ni-NTA resin containing RsbV-^{32}P was then exchanged into 50 mM K•HEPES pH 8.0, 100 mM NaCl buffer using 3 subsequent Zeba spin columns to remove all unincorporated nucleotide and free phosphate. Labeled RsbV-^{32}P was aliquoted and frozen at -80ºC for future use.

All phosphatase assays were performed at room temperature in 50 mM K•HEPES pH 7.5, 100 mM NaCl. The concentrations of enzyme, substrate, $MnCl_2$, and $MgCl_2$ were varied as indicated. 10 µM RsbT was additionally added to reactions as indicated. Reactions were stopped with 0.5 M EDTA, pH 8.0 and run on PEI-Cellulose TLC plates developed in 1 M $LiCl_2$ and 0.8 M acetic acid and imaged on a Typhoon scanner. Phosphatase assays were performed more than three independent times as separate experiments. Data shown in figures is from a single representative experiment, and reported errors are the error from the fit.

***B. subtilis* strain construction**

B. subtilis cells were grown in Lennox lysogeny broth (LB, Sigma Aldrich) as liquid medium or as plates supplemented with 15% Bacto Agar (Difco). Antibiotics were used as appropriate for

maintenance of plasmids or for selection of transformants: MLS (50 µg/ml erythromycin, 250 µg/ml lincomycin), kanamycin (10 µg/ml). For plates used to visualize σ^B reporter activity, 80 µg/ml of 5-bromo-4-chloro-3-indolyl-β-D-galactopyranoside (X-gal) and 1 mM IPTG were added. All *B. subtilis* strains were derived from the PY79 strain background and are listed in the table of strains. Plasmids based on pHB201(Bron et al. 1998) were introduced to *B. subtilis* strains using natural competence(Harwood & Cutting 1990).

Genetic screens

Genetic screens were performed as described previously (Ho & Bradshaw 2021). Plasmids containing *rsbU* or *rsbT/rsbU*^{Y28I} were subjected to PCR mutagenesis using GoTaq DNA polymerase mix (Promega) supplemented with 2mM additional $MgCl_2$. Pools of mutagenized inserts were assembled into digested plasmid using isothermal (Gibson) assembly and transformed into *E. coli* DH5α cells. Mutation rate of approximately one single-nucleotide polymorphism per kilobase of DNA was confirmed by sequencing individual clones. Plasmids were then introduced to *B. subtilis* using natural competence and cells were plated on selective medium containing IPTG and X-gal for two days at 37ºC. Blue colonies were selected, restruck on plates with and without IPTG, and plasmids recovered from single colonies that retested as σ^B positive were sequenced using Sanger sequencing. For the RsbU^{Y28I} suppressor screen, two independent pools of PCR mutagenized plasmid were screened. In addition to the reported variants that were selected, we identified simple revertants that restored Y28 in both pools, and mutations in the promoter and RBS that we predict enhanced protein production. These variants were not studied further. Individual amino acid changing mutations were rebuilt in the parental

plasmid using PCR (QuickChange) mutagenesis and the phenotypes were validated by replating on indicator plates. All strains shown in the figures are from these rebuilt plasmids.

AlphaFold2 structure predictions

AlphaFold2 predictions were performed using ColabFold (Mirdita et al. 2022). Alphafold2_multimer_v2 was used in unpaired_paired mode with no templates with 3 recycles, 200 iterations, and greedy pairing strategy. The predicted aligned error plots for all AlphaFold2 structures are shown in Figure S8.

References

Battesti, A. et al., 2013. Anti-adaptors provide multiple modes for regulation of the RssB adaptor protein. *Genes & development*, 27(24), pp.2722–2735.

Battesti, A., Majdalani, N. & Gottesman, S., 2011. The RpoS-mediated general stress response in Escherichia coli. *Annual review of microbiology*, 65, pp.189–213.

Bergkessel, M., Basta, D.W. & Newman, D.K., 2016. The physiology of growth arrest: uniting molecular and environmental microbiology. *Nature Reviews Microbiology*, 14(9), pp.549–562.

Bilwes, A.M. et al., 1999. Structure of CheA, a signal-transducing histidine kinase. *Cell*, 96(1), pp.131–141.

Boekhoud, I.M. et al., 2020. Redefining the Clostridioides difficile σB Regulon: σB Activates Genes Involved in Detoxifying Radicals That Can Result from the Exposure to Antimicrobials and Hydrogen Peroxide. *mSphere*, 5(5).

Boylan, S.A., Redfield, A.R. & Price, C.W., 1993. Transcription factor sigma B of Bacillus subtilis controls a large stationary-phase regulon. *Journal of Bacteriology*, 175(13), pp.3957–3963.

Bradshaw, N. et al., 2017. A widespread family of serine/threonine protein phosphatases shares a common regulatory switch with proteasomal proteases. *eLife*, 6.

Brody, M.S., Stewart, V. & Price, C.W., 2009. Bypass suppression analysis maps the signalling pathway within a multidomain protein: the RsbP energy stress phosphatase 2C from Bacillus subtilis. *Molecular microbiology*, 72(5), pp.1221–1234.

Bron, S. et al., 1998. Protein secretion and possible roles for multiple signal peptidases for precursor processing in bacilli. *Journal of biotechnology*, 64(1), pp.3–13.

Brugger, C., Schwartz, J., et al., 2023. Structure of phosphorylated-like RssB, the adaptor delivering σs to the ClpXP proteolytic machinery, reveals an interface switch for activation. *The Journal of biological chemistry*, 299(12), p.105440.

Brugger, C., Srirangam, S. & Deaconescu, A.M., 2023. IraM Remodels the RssB Segmented Helical Linker to Stabilize σs Against Degradation by ClpXP. *The Journal of biological chemistry*, p.105568.

Cordeiro, T.N. et al., 2017. Structural Characterization of Highly Flexible Proteins by Small-Angle Scattering. *Advances in experimental medicine and biology*, 1009, pp.107–129.

de Been, M. et al., 2010. A novel hybrid kinase is essential for regulating the sigma(B)-mediated stress response of Bacillus cereus. *Environmental microbiology*, 12(3), pp.730–745.

Delumeau, O. et al., 2004. Functional and structural characterization of RsbU, a stress signaling protein phosphatase 2C. 279(39), pp.40927–40937.

Dorich, V. et al., 2019. Structural basis for inhibition of a response regulator of σS stability by a ClpXP antiadaptor. *Genes & development*, 33(11-12), pp.718–732.

Fernández Martínez, L. et al., 2009. Osmoregulation in Streptomyces coelicolor: modulation of SigB activity by OsaC. *Molecular microbiology*, 71(5), pp.1250–1262.

Galperin, M.Y., 2006. Structural classification of bacterial response regulators: diversity of output domains and domain combinations., 188(12), pp.4169–4182.

Gottesman, S., 2019. Trouble is coming: Signaling pathways that regulate general stress responses in bacteria.

Gourinchas, G. et al., 2017. Long-range allosteric signaling in red light-regulated diguanylyl cyclases. *Science advances*, 3(3), p.e1602498.

Greenstein, A.E. et al., 2009. Interdomain communication in the Mycobacterium tuberculosis environmental phosphatase Rv1364c., 284(43), pp.29828–29835.

Grigoryan, G. & DeGrado, W.F., 2011. Probing designability via a generalized model of helical bundle geometry. *Journal of Molecular Biology*, 405(4), pp.1079–1100.

Guerreiro, D.N., Arcari, T. & O'Byrne, C.P., 2020. The σB-Mediated General Stress Response of Listeria monocytogenes: Life and Death Decision Making in a Pathogen. *Frontiers in microbiology*, 11, p.1505.

Haldenwang, W.G. & Losick, R., 1979. A modified RNA polymerase transcribes a cloned gene under sporulation control in Bacillus subtilis. *Nature*, 282(5736), pp.256–260.

Hardwick, S.W. et al., 2007. Structural and functional characterization of partner switching regulating the environmental stress response in Bacillus subtilis. 282(15), pp.11562–11572.

Harwood, C.R. & Cutting, S.M., 1990. Molecular Biological Methods for Bacillus. pp.1–308.

Hecker, M., Pané-Farré, J. & Völker, U., 2007. SigB-dependent general stress response in Bacillus subtilis and related gram-positive bacteria. *Annual review of microbiology*, 61, pp.215–236.

Heinz, V. et al., 2022. The Vibrio vulnificus stressosome is an oxygen-sensor involved in regulating iron metabolism. *Communications biology*, 5(1), p.622.

Herbert, S. et al., 2010. Repair of global regulators in Staphylococcus aureus 8325 and comparative analysis with other clinical isolates. *Infection and immunity*, 78(6), pp.2877–2889.

Ho, K. & Bradshaw, N., 2021. A conserved allosteric element controls specificity and activity of functionally divergent PP2C phosphatases from B. subtilis. *The Journal of biological chemistry*, p.100518.

Hopkins, J.B., 2024. BioXTAS RAW 2: new developments for a free open-source program for small-angle scattering data reduction and analysis. *Journal of applied crystallography*, 57(Pt 1), pp.194–208.

Hopkins, J.B., Gillilan, R.E. & Skou, S., 2017. BioXTAS RAW: improvements to a free open-source program for small-angle X-ray scattering data reduction and analysis. *Journal of applied crystallography*, 50(Pt 5), pp.1545–1553.

Jumper, J. et al., 2021. Highly accurate protein structure prediction with AlphaFold. *Nature*, 596(7873), pp.583–589.

Kikhney, A.G. & Svergun, D.I., 2015. A practical guide to small angle X-ray scattering (SAXS) of flexible and intrinsically disordered proteins. *FEBS letters*, 589(19 Pt A), pp.2570–2577.

Kint, N. et al., 2019. The σB signalling activation pathway in the enteropathogen Clostridioides difficile. *Environmental microbiology*, 21(8), pp.2852–2870.

Kirby, N. et al., 2016. Improved radiation dose efficiency in solution SAXS using a sheath flow sample environment. *Acta crystallographica. Section D, Structural biology*, 72(Pt 12), pp.1254–1266.

Kumar, P. & Woolfson, D.N., 2021. Socket2: a program for locating, visualizing and analyzing coiled-coil interfaces in protein structures. *Bioinformatics (Oxford, England)*, 37(23), pp.4575–4577.

Manalastas-Cantos, K. et al., 2021. ATSAS 3.0: expanded functionality and new tools for small-angle scattering data analysis. *Journal of applied crystallography*, 54(Pt 1), pp.343–355.

Marles-Wright, J. et al., 2008. Molecular architecture of the “stressosome,” a signal integration and transduction hub., 322(5898), pp.92–96.

Meisburger, S.P. et al., 2016. Domain Movements upon Activation of Phenylalanine Hydroxylase Characterized by Crystallography and Chromatography-Coupled Small-Angle X-ray Scattering. *Journal of the American Chemical Society*, 138(20), pp.6506–6516.

Mirdita, M. et al., 2022. ColabFold: making protein folding accessible to all. *Nature methods*, 19(6), pp.679–682.

Mittenhuber, G., 2002. A phylogenomic study of the general stress response sigma factor sigmaB of Bacillus subtilis and its regulatory proteins. *Journal of Molecular Microbiology and Biotechnology*, 4(4), pp.427–452.

Möglich, A., Ayers, R.A. & Moffat, K., 2009. Structure and signaling mechanism of Per-ARNT-Sim domains. *Structure (London, England : 1993)*, 17(10), pp.1282–1294.

Nadezhdin, E.V., Brody, M.S. & Price, C.W., 2011. An α/β Hydrolase and Associated Per-ARNT-Sim Domain Comprise a Bipartite Sensing Module Coupled with Diverse Output Domains. *PLoS ONE*, 6(9), p.e25418.

Quin, M.B. et al., 2012. The bacterial stressosome: a modular system that has been adapted to control secondary messenger signaling. *Structure (London, England : 1993)*, 20(2), pp.350–363.

Rambo, R.P. & Tainer, J.A., 2011. Characterizing flexible and intrinsically unstructured biological macromolecules by SAS using the Porod-Debye law. *Biopolymers*, 95(8), pp.559–571.

Randall, T.E. et al., 2022. Sensory Perception in Bacterial Cyclic Diguanylate Signal Transduction. *Journal of Bacteriology*, 204(2), p.e0043321.

Receveur-Bréchot, V. & Durand, D., 2012. How random are intrinsically disordered proteins? A small angle scattering perspective. *Current protein & peptide science*, 13(1), pp.55–75.

Rodríguez-Martínez, K. et al., 2023. Defining the regulatory mechanisms of sigma factor RpoS degradation in Azotobacter vinelandii and Pseudomonas aeruginosa. *Molecular microbiology*, 120(1), pp.91–102.

Schneidman-Duhovny, D. et al., 2013. Accurate SAXS profile computation and its assessment by contrast variation experiments. *Biophysical journal*, 105(4), pp.962–974.

Schneidman-Duhovny, D. et al., 2016. FoXS, FoXSDock and MultiFoXS: Single-state and multi-state structural modeling of proteins and their complexes based on SAXS profiles. *Nucleic Acids Research*, 44(W1), pp.W424–9.

Svergun, D.I., 1992. Determination of the regularization parameter in indirect-transform methods using perceptual criteria. *Journal of applied crystallography*, 25, pp.495–503.

Trewhella, J. et al., 2017. 2017 publication guidelines for structural modelling of small-angle scattering data from biomolecules in solution: an update. *Acta crystallographica. Section D, Structural biology*, 73(Pt 9), pp.710–728.

Tuchscherr, L. & Löffler, B., 2016. Staphylococcus aureus dynamically adapts global regulators and virulence factor expression in the course from acute to chronic infection. *Current genetics*, 62(1), pp.15–17.

Vijay, K. et al., 2000. A PP2C phosphatase containing a PAS domain is required to convey signals of energy stress to the sigmaB transcription factor of Bacillus subtilis. *Molecular microbiology*, 35(1), pp.180–188.

Yang, X. et al., 1996. Opposing pairs of serine protein kinases and phosphatases transmit signals of environmental stress to activate a bacterial transcription factor. *Genes & development*, 10(18), pp.2265–2275.

1080 Zschiedrich, C.P., Keidel, V. & Szurmant, H., 2016. Molecular Mechanisms of Two-Component
1081 Signal Transduction. *Journal of Molecular Biology*, 428(19), pp.3752–3775.

Figure 1

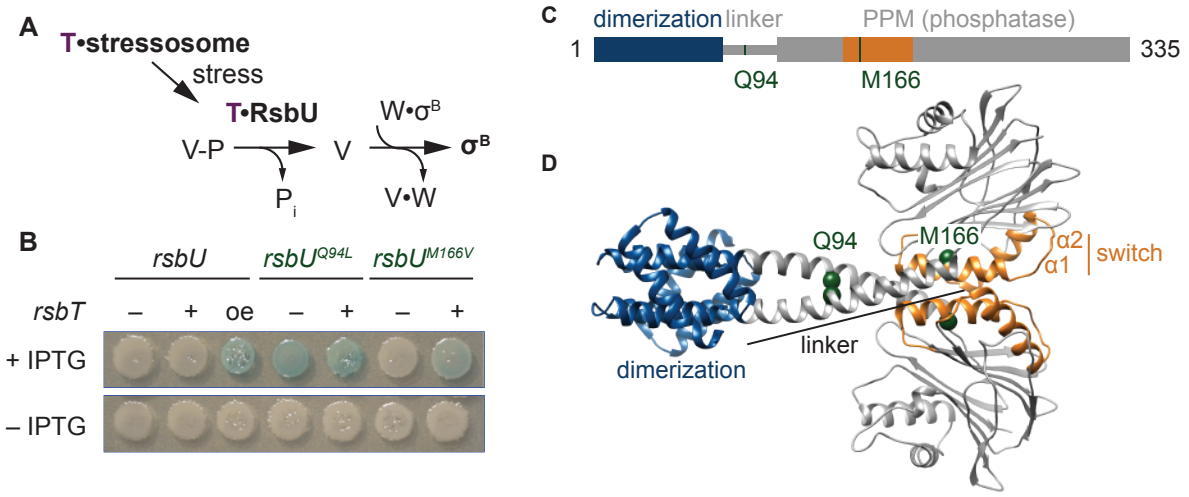

Figure 1: The linker controls RsbU activation through a conserved switch element
A Reaction scheme of the RsbU dependent pathway of the environmental stress response. RsbU is activated by its partner protein RsbT (T, purple) to dephosphorylate its substrate protein RsbV-P (V-P). This displaces the GSR alternative sigma factor σ^B from inhibition by the anti-sigma factor RsbW (W) to initiate transcription of σ^B dependent genes (bold). **B** Amino acid substitutions in RsbU (Q94L and M166V) cause enhanced σ^B activity in *B. subtilis*. Strains carrying a lacZ reporter of σ^B activity (*ctc-lacZ*) were plated on X-gal indicator plates in the presence (top) or absence (bottom) of IPTG to induce expression of the *rsbU* constructs. Strains assayed either were deleted for *rsbT* at the chromosomal locus (–) or retained the chromosomal copy of *rsbT* (+). A control strain in which *rsbT* was additionally overexpressed on the plasmid with *rsbU* is indicated by oe. Plates were imaged after 24 hours of growth at 37ºC, which was shorter than the time used to visualize *lacZ* expression from the $rsbU^{M166V}$ strain previously(Ho & Bradshaw 2021). **C** Domain diagram of RsbU. The N-terminal domain of RsbU (blue) (amino acids 1-81) is joined to the α-helical linker domain (grey) (82-112), which connects it to the PPM phosphatase domain (grey) (121-335). The regulatory switch element of the PPM phosphatase domain is colored orange (156-201). The N-terminal domain contains the putative RsbT binding site and the catalytic and metal coordination site is contained in the phosphatase domain. The location of RsbT-bypass mutations are highlighted in green. **D** AlphaFold2 model of RsbU dimer. The N-terminal domains (blue), α-helical linkers (grey), and phosphatase domains (grey) are labeled, with the regulatory switch elements (α1 and α2) colored orange. The Cα atoms of residues Q94 and M166 are shown in green spheres.

Figure 2

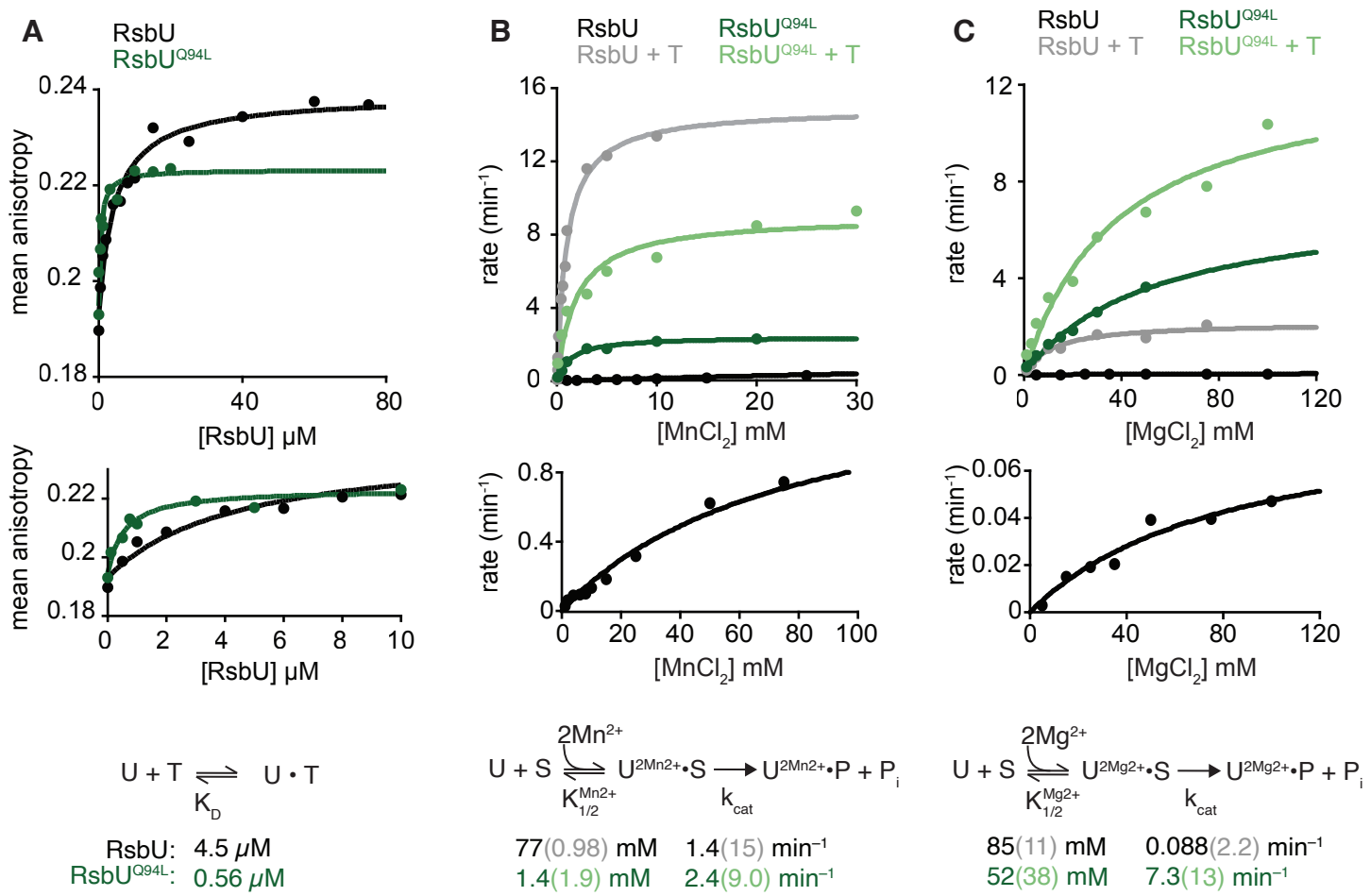

Figure 2: RsbU linker influences RsbT binding and phosphatase activity

A Mean anisotropy of RsbT-TMR (200 nM) is plotted as a function of RsbU concentration. The curves are fits to a quadratic binding equation using non-linear curve fitting. Wild-type RsbU (black) has a K_D of 4.5 ± 0.96 μM and RsbU^{Q94L} (green) has a K_D of 0.56 ± 0.15 μM. The lower plot is an inset of RsbU concentrations to 10 μM. Below is the reaction scheme of RsbT binding to RsbU with the values for the calculated K_D below. **B** The rate of dephosphorylation of RsbV-P is plotted as a function of concentration of $MnCl_2$. Observed rates for RsbU in the presence (black) and absence (grey) of RsbT and RsbU^{Q94L} in the presence (green) and absence (light green) of RsbT are shown. Curves are fits to the Michaelis-Menten equation using non-linear curve fitting. The k_{cat} of wild-type RsbU is 15 ± 0.35 min^{-1} with RsbT and 1.4 ± 0.077 min^{-1} without RsbT and the k_{cat} of RsbU^{Q94L} is 9.0 ± 0.64 min^{-1} with RsbT and 2.4 ± 0.084 min^{-1} without RsbT. The K_M^{MnCl2} of wild-type RsbU is 0.98 ± 0.069 mM with RsbT and 77 ± 9.0 mM without RsbT and the K_M^{MnCl2} of RsbU^{Q94L} is 1.4 ± 0.19 mM with RsbT and 1.9 ± 0.56 mM without RsbT. The lower plot is an inset of wild-type RsbU in the absence of RsbT of $MnCl_2$ concentrations to 100 mM. Below is a summary of a reaction scheme of RsbU dephosphorylating RsbV-P (denoted as S) with Mn^{2+} cofactor, with the K_M^{MnCl2} and k_{cat} values below. Data for RsbU are reproduced from (Ho & Bradshaw 2021). **C** The rate of dephosphorylation of RsbV-P is plotted as a function of concentration of $MgCl^2$. Data and curve fits are colored as in **B**. Non-linear curve fits to the Michaelis-Menten equation gave k_{cat} of wild-type RsbU 2.2 ± 0.16 min^{-1} with RsbT and 0.088 ± 0.023 min^{-1} without RsbT and k_{cat} of RsbU^{Q94L} 13 ± 1.1 min^{-1} with RsbT and 7.3 ± 1.2 min^{-1} without RsbT. The K_M^{MgCl2} of wild-type RsbU is 11 ± 2.6 mM with RsbT and 85 ± 38 mM without RsbT, and the K_M^{MgCl2} RsbU^{Q94L} is 38 ± 8.4 mM with RsbT and 52 ± 14 mM without RsbT. The lower plot is an inset of wild-type RsbU in the absence of RsbT. Below is a summary of a reaction scheme of RsbU dephosphorylating RsbV-P (denoted as S) with Mg^{2+} cofactor, with the K_M^{MgCl2} and k_{cat} calculated values below.

Figure 3

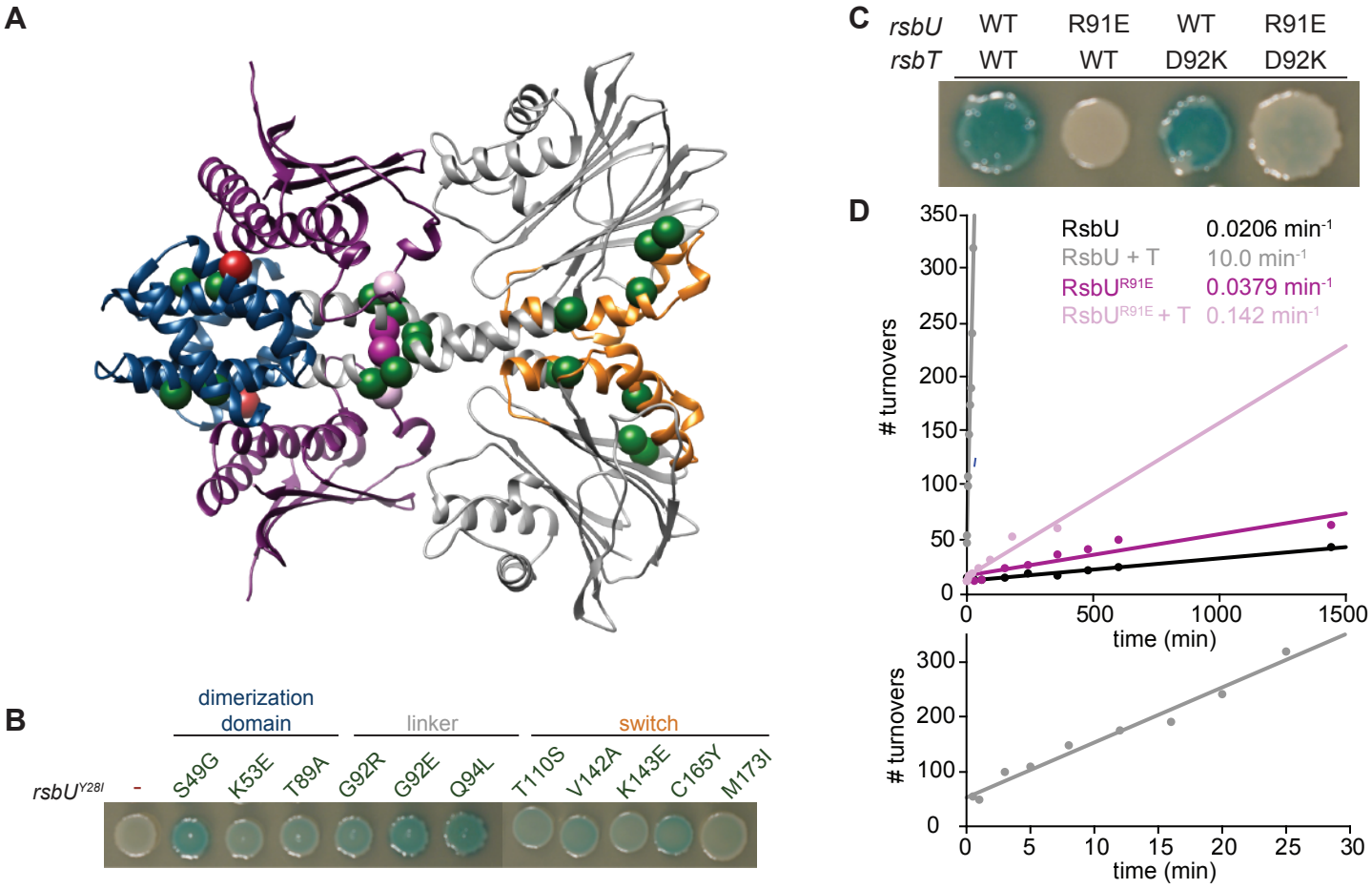

Figure 3: RsbT has a hybrid interface with RsbU N-terminal dimerization domain and linker

A An AlphaFold2 model of a heterotetrameric 2RsbT/2RsbU complex is shown in ribbon representation. RsbT (purple) binds with an interface that spans the N-terminal domains (blue) and α-helical linkers (grey) of both RsbU protomers. The PPM phosphatase domains are colored grey and the regulatory switch elements (α1 and α2) are colored orange. The Cα position of $RsbU^{Y28}$ is shown as a red sphere, and the Cα position of $rsbU^{Y28I}$ suppressor substitutions are shown as green spheres. The Cα position of $RsbU^{R91}$ (dark) and $RsbT^{D92}$ (light) are shown as pink spheres. **B** Strains with a σ^B LacZ reporter were plated on IPTG/X-gal plates to induce expression of plasmid borne *rsbT* and $rsbU^{Y28I}$ and visualize σ^B activity (indicated by blue pigmentation after 24 hours of growth at 37ºC). Additional amino acid substitutions in the *rsbU* gene are indicated above the spots, with the region where they are located in the RsbU structure specified. **C** Strains with a σ^B LacZ reporter were plated on IPTG/X-gal plates to induce expression of plasmid borne *rsbT* and *rsbU* with indicated changes to the RsbT and RsbU amino acid sequence. Plates were imaged after 36 hours of growth at 37ºC to allow the blue pigmentation from $rsbU^{R91E}/rsbT^{D92K}$ expressing cells to be more visible. **D** R91E does not decrease the basal phosphatase activity of RsbU. Plots show dephosphorylation of RsbV-P (25 μM) by RsbU (black) and $RsbU^{R91E}$ (pink) (0.5μM) in the presence of 10 mM $MnCl^2$ and the presence or absence of 10 μM RsbT (lite colors) as a function of time. Linear fits of the data are shown, with the slopes indicating the observed rates (k_{obs}). The k_{obs} for wild-type RsbU is 0.0206 ± 0.00124 min^{-1} without RsbT and 10.0 ± 0.628 min^{-1} with RsbT. The k_{obs} for $RsbU^{R91E}$ is 0.0379 ± 0.00543 min^{-1} without RsbT and 0.142 ± 0.0161 min^{-1} with RsbT. The lower plot is an inset of wild-type RsbU in the presence of RsbT to thirty minutes.

Figure 4

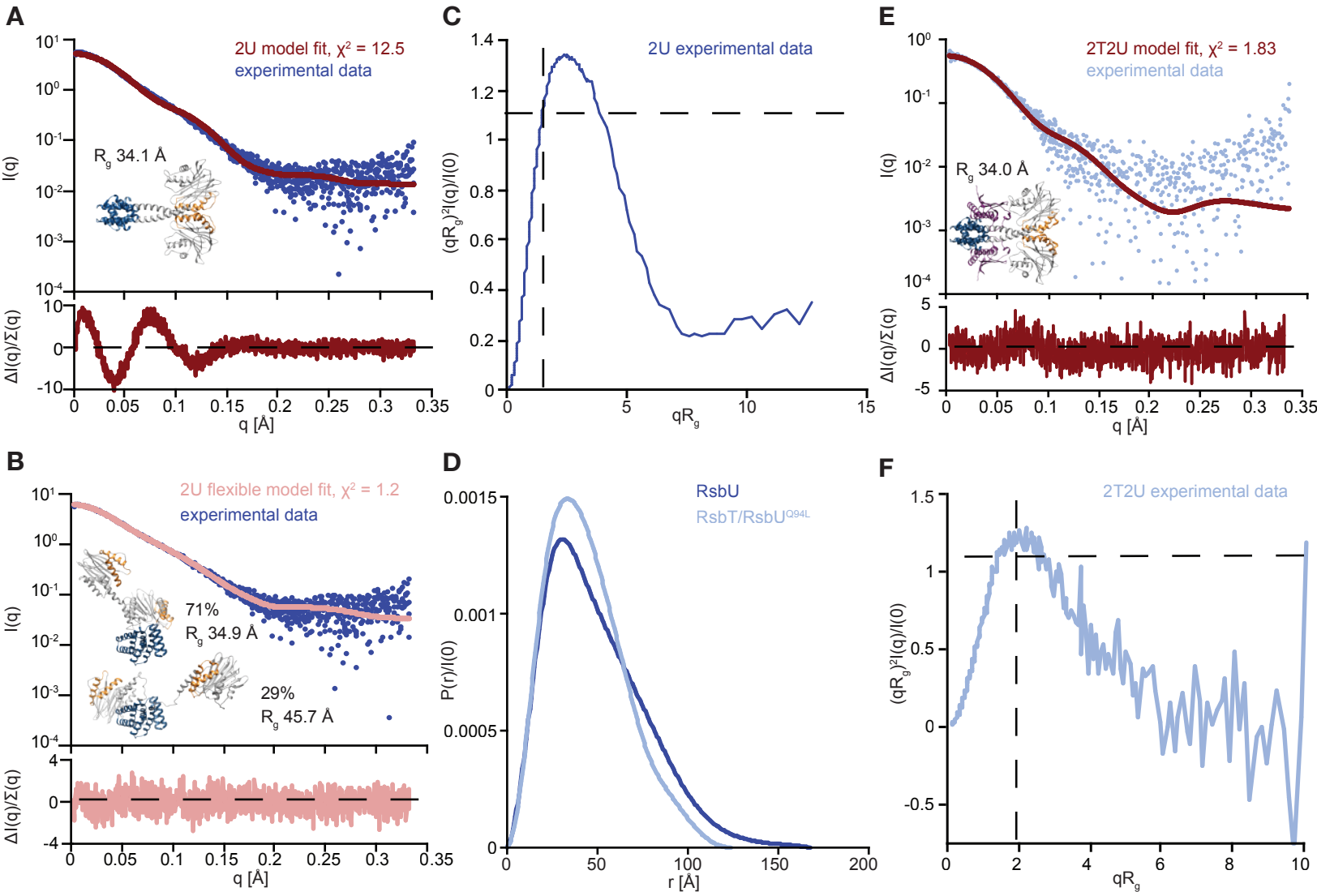

Figure 4: RsbU linker is flexible in the absence of RsbT, and is rigidified by RsbT binding.
A I(q) versus q plot of the dimer component of SAXS scattering data from RsbU (blue) overlaid with a FoXS generated profile fit of the AlphaFold2 RsbU dimer structure (red). The upper plot shows I(q) versus q on log-linear axes while the lower plot shows the uncertainty normalized residuals of the fit ((experimental-computed)/error), χ2 of 12.53. The AlphaFold2 model used for the fit is shown inset. **B** I(q) versus q plot of the dimer component of SAXS scattering data from RsbU (blue) overlaid with a MultiFoXS generated two-state profile fit with flexibility allowed for residues 82-96 (pink). The upper plot shows I(q) versus q on log-linear axes while the lower plot shows the uncertainty normalized residuals of the fit ((experimental-computed)/error), χ2 of 1.2. The two best fit flexible models are shown with R_g and percentage of each model used in the fit indicated. **C** Dimensionless Kratky plot of SAXS scattering data from the dimer component of RsbU experimental data (blue). The experimental profile was logarthmically binned to reduce noise at high qR_g. **D** Normalized P(r) by I(0) versus r plot from SAXS scattering data from the dimer component of RsbU (blue) and heterotetrameric component of RsbT/RsbU^{Q94L} complex (light blue). **E** I(q) versus q plot of the heterotetrameric component of SAXS scattering data from RsbT/RsbU^{Q94L} complex (blue) overlaid with a FoXS generated profile fit of the AlphaFold2 RsbT/RsbU heterotetramer structure (red). The upper plot show I(q) versus q on a log-linear axes while the lower plot shows the uncertainty normalized residuals of the fits ((experimental-computed)/error), χ2 of 1.83. The RsbT/RsbU AlphaFold2 model used in the fit is shown as an inset. F Dimensionless Kratky plot of SAXS scattering data from the heterotetrameric component of RsbT/RsbU^{Q94L} complex experimental data (blue). The experimental profile was binned logarithmically to reduce noise at high qR_g values.

Figure 5

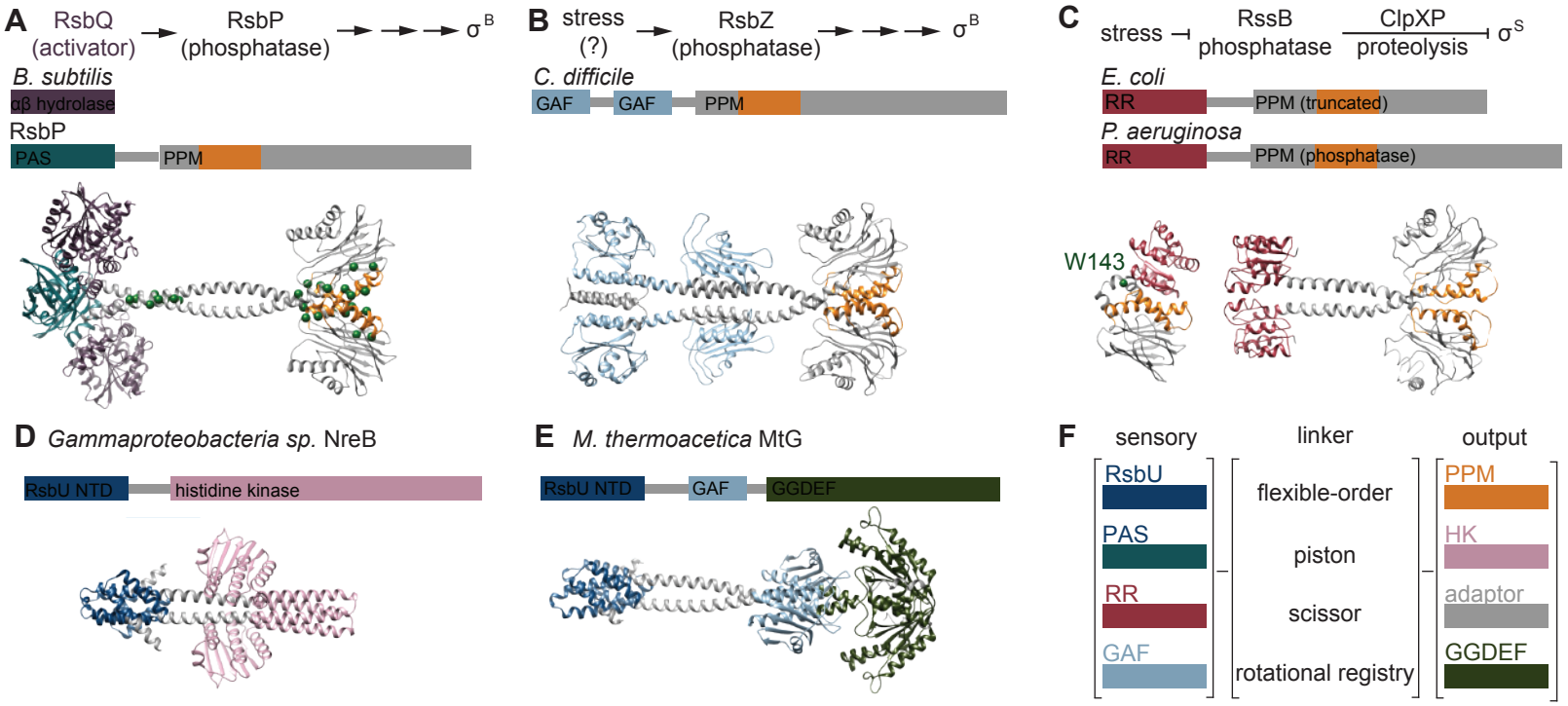

Figure 5: An exchangeable toolkit for bacterial signal transduction

A An AlphaFold2 model of the *B. subtilis* energy stress phosphatase RsbP is shown bound to its activating α/β-hydrolase protein RsbQ (purple) with a schematic of the σB activation pathway shown above. RsbP has an N-terminal PAS domain (turquoise) that is connected to the PPM phosphatase domain by a predicted coiled coil linker. The Cα positions of bypass suppressor mutations that render RsbP active in the absence of RsbQ(Brody et al. 2009) are shown as green spheres. The switch element of the PPM phosphatase domain (α1 and α2) is colored orange. **B** An AlphaFold2 model of the *C. difficile* GSR phosphatase RsbZ is shown with a schematic of the σ^B activation pathway shown above. RsbZ has tandem N-terminal GAF domains (blue) that connect to the PPM phosphatase domain by a predicted coiled coil linker. The switch element of the PPM phosphatase domain (α1 and α2) is colored orange. **C** Experimental structures of the GSR initiating adaptor protein RssB from *E. coli* (left, 8T85) and *P. aeruginosa* (right, 3F7A) are shown with a schematic of the σ^S activation pathway shown above. The Cα positions of a bypass suppressor mutation (W143R) that renders RssB insensitive to anti-adapter proteins is shown as a green sphere. The switch element of the PPM phosphatase domain (α1 and α2) is colored orange. **D** An AlphaFold2 model of a dimer of the histidine kinase NreB from a *Gammaproteobacteria* species (MBI3545564.1) is shown with the RsbU N-terminal domain colored blue and the histidine kinase domain colored pink. **E** An AlphaFold2 model of a dimer of the GGDEF diguanylate cyclase MtG from *M. thermoacetica* (WP_011392981.1) is shown with RsbU N-terminal domain colored blue, GAF domain colored lite blue, and GGDEF domain colored green. **F** Schematic illustrating how various sensor domains (RsbU N-terminal dimerization domain, PAS, response receiver (RR), and GAF) can control various output activities (serine/threonine phosphatase (PPM), histidine kinase (HK), protease adaptor, and diguanylate cyclase (GGDEF). We hypothesize that the shared regulatory mechanism through a dimeric coiled-coil linker makes these regulatory domains modularly exchangeable across effector domains. Known mechanisms for how allosteric regulation is transmitted through the linker are listed.

Supplemenal Figure 1

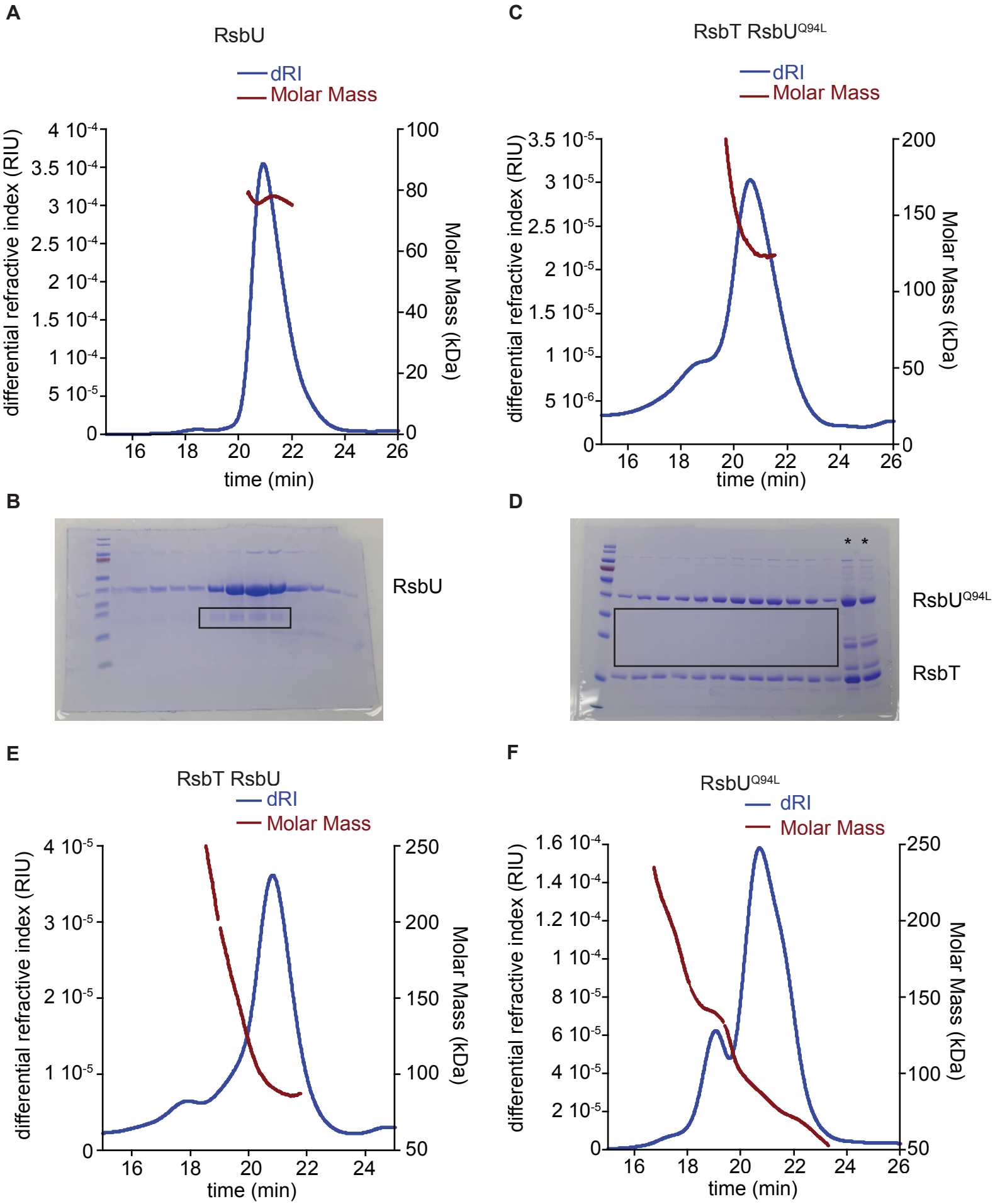

Supplemental Figure 1: MALS estimate of molecular weight of RsbU dimer, RsbT/RsbUQ94L complex, RsbT/RsbU complex, and RsbUQ94L

A Plot of inline SEC-MALS analysis of RsbU with measured differential refractive index (blue, left axis) and the molecular weight calculated from MALS (red, right axis). **B** Denaturing SDS-PAGE gel of successive fractions from the equivalent range of the elution as shown in A from preparative size exclusion chromatography of the sample of RsbU used for SEC-MALS-SAXS. Black box denotes the C-terminal truncation product present in each lane of the main peak. **C** Plots from inline SEC-MALS analysis of RsbT/RsbU^{Q94L} complex with measured differential refractive index (blue, left axis) and the molecular weight calculated from MALS (red, right axis). **D** Denaturing SDS-PAGE gel of successive fractions from the equivalent range of the elution of RsbT/U^{Q94L} as shown in C from preparative size exclusion chromatography of the sample used for SEC-MALS-SAXS. Black box denotes lack of C-terminal truncation product during co-expression and purification of RsbT/RsbU^{Q94L} complex. * Denotes load samples on gel. **E** Plots from inline SEC-MALS analysis of RsbT/U complex with measured differential refractive index (blue, left axis) and the molecular weight calculated from MALS (red, right axis). **F** Plot inline SEC-MALS analysis of RsbU^{Q94L} with measured differential refractive index (blue, left axis) and the molecular weight calculated from MALS (red, right axis).

Supplemental Figure 2

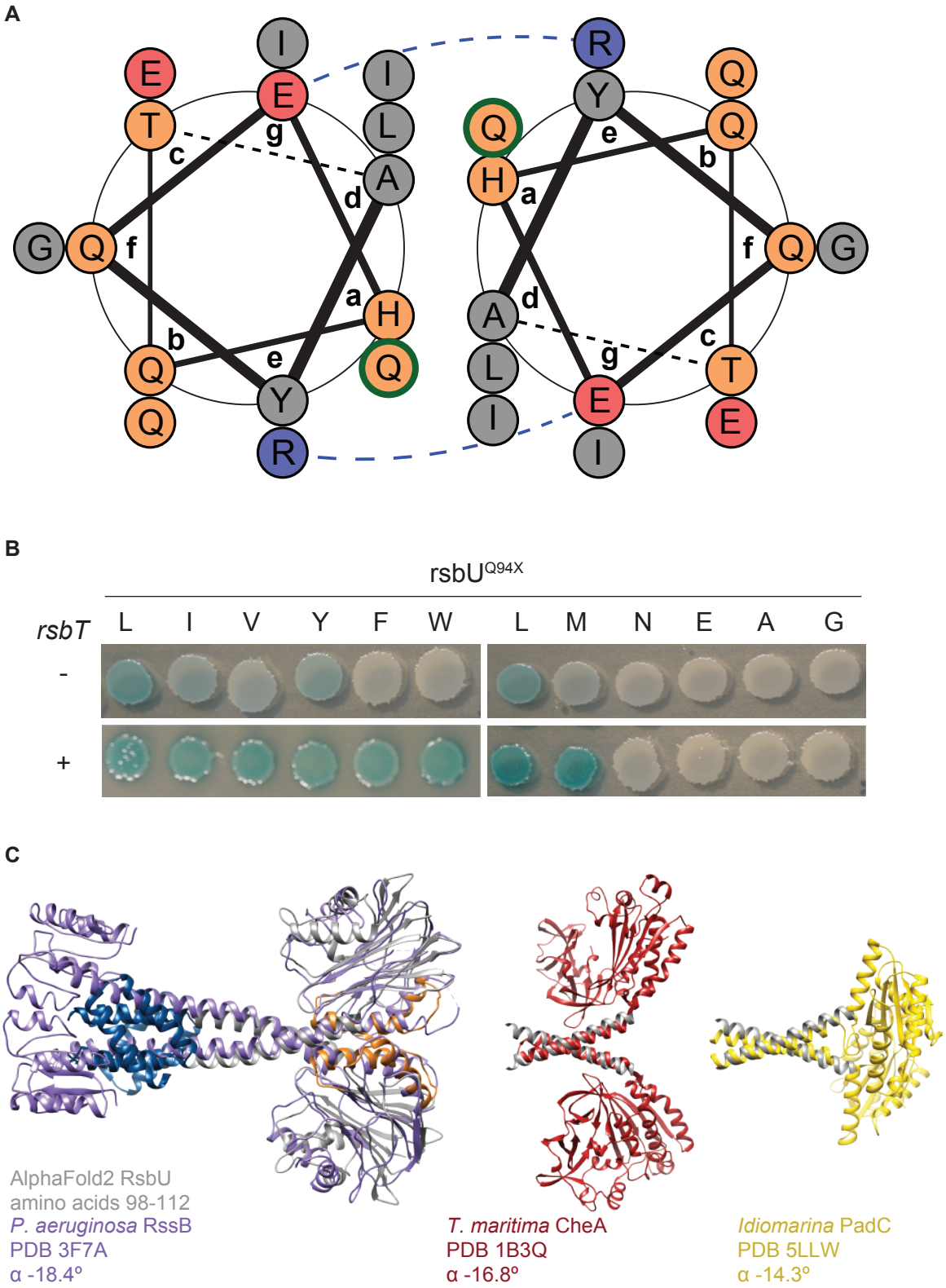

Supplemental Figure 2: Q94L stabilizes the packing interface of the coiled-coil of the linker

A Coil diagram of RsbU residues 83-97 generated using DrawCoil. Grey circles indicate non-polar residues, orange indicate polar residues, red indicate negatively charged residues, and blue indicate positively charged residues. The blue dashed line depicts a putative salt bridge. Residue Q94 (circled in green) sits in the interface of the coils and is shown packing with L90. **B** An allelic series of amino acid substitutions at position 94 of RsbU was generated in an *rsbU* expression plasmid. Plasmids were introduced into *B. subtilis* cells containing a LacZ reporter of σ^B activity that were deleted for *rsbT* (top) or with *rsbT* retained on the chromosome (bottom). Cells were plated on IPTG/X-gal plates to induce *rsbU* expression and to indicate σ^B activity (blue pigmentation). **C** α-helical pitch analysis of coiled-coil domains. The AlphaFold2 model of an RsbU dimer is overlayed with crystal structure of *P. aeruginosa* RssB (PDB 3F7A, purple, left). The helical linker region extending out of the coiled coil (RsbU98-112) is shown (grey) overlaid with *T. maritima* transducing histidine kinase CheA (PDB 1B3Q, red, middle) and *Idiomarina* A28L diguanylyl cyclases PadC (PDB 5LLW, yellow, right). α angles from Crick parameterization analysis using CCCP are shown for the overlaid region.

Supplemental Figure 3

A

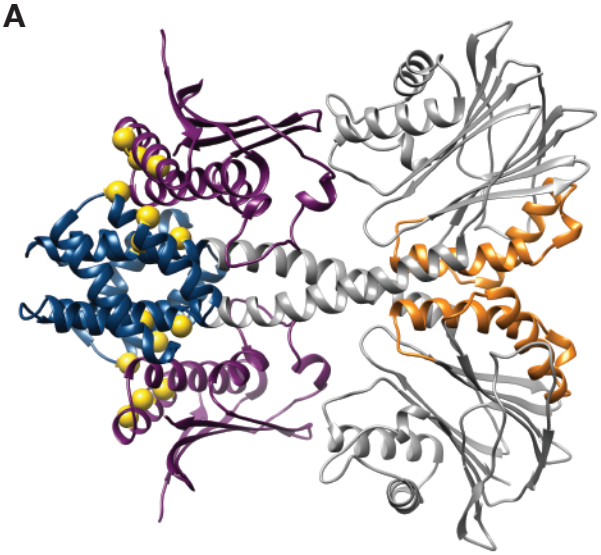

B

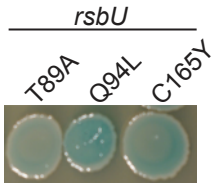

Supplemental Figure 3: RsbT binds to the linker

A Interface of RsbT and N-terminal domain of RsbU. A ribbon representation is shown of the AlphaFold2 model of the heterotetrameric 2RsbT/2RsbU complex with RsbU N-terminal dimerization domain colored blue, the switch element of the PPM domain (α1 and α2) colored orange, and RsbT colored purple. The Cα of positions of amino acids implicated in the binding interface of RsbT and RsbU N-terminal dimerization domain(Hardwick et al. 2007) are represented on the AlphaFold2 structure as yellow spheres. **B** Strains with a σB LacZ reporter (*ctc-lacZ*) are shown plated on IPTG/X-gal plates to induce expression of rsbU with the indicated amino acid substitutions. *rsbU* was chromosomally deleted, but *rsbT* was retained at its native locus. σ^B activity is visualized by the blue pigment after 36 hours of growth at 37ºC.

Supplemental Figure 4

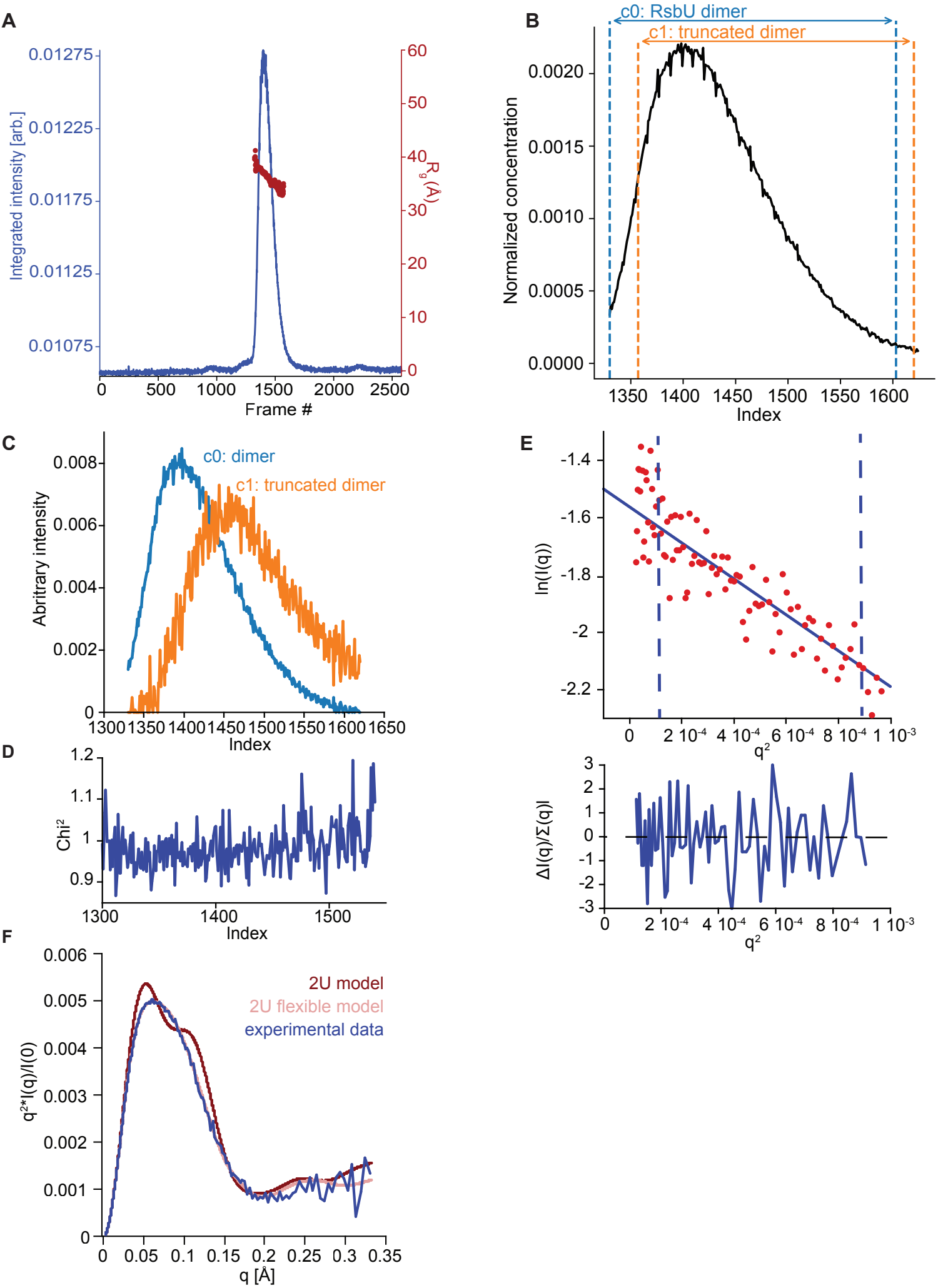

Supplemental Figure 4: EFA deconvolution and Guinier analysis of RsbU dimer SAXS profiles

A SAXS data summary for RsbU. Series intensity (blue, left axis) versus frames, and R_g versus frame (red, right axis) are plotted. **B** The selected intensity range for EFA (black) (frame index 1330-1620), and the individual component ranges for deconvolution; blue denotes the range of frames where the scattering component we assigned as the c0, RsbU dimer, was detected (frame index 1330-1603) and orange denotes the range of frames where the scattering component that is c1, presumably from a RsbU heterodimer containing a c-terminal truncation product dimer (frame index 1357-1620). **C** Area normalized concentration profiles for the c0, RsbU dimer component (blue) and c1, RsbU heterodimer containing c-terminal truncation product dimer (orange). **D** Mean $\chi 2$ values for the fit of the EFA deconvolution to the original scattering data. **E** Guinier fit for RsbU dimer component on the upper plot and uncertainty normalized residuals of the fit on the lower plot. The scattering data for the dimer component (red) is fit to the Guinier approximation (blue). The blue dashed lines are the q_{min} and q_{max} at values 0.00356 Å-1 and 0.0234 Å-1, respectively. **F** Kratky plot of SAXS scattering data from the dimer component of RsbU experimental data (blue) overlaid with the profile computed by FoXS based on the AlphaFold2 model of an RsbU dimer (red) and the profile of the flexible model computed by MultiFoXS (pink). The experimental profile was logarthmically binned to reduce noise at high q.

Supplemental Figure 5

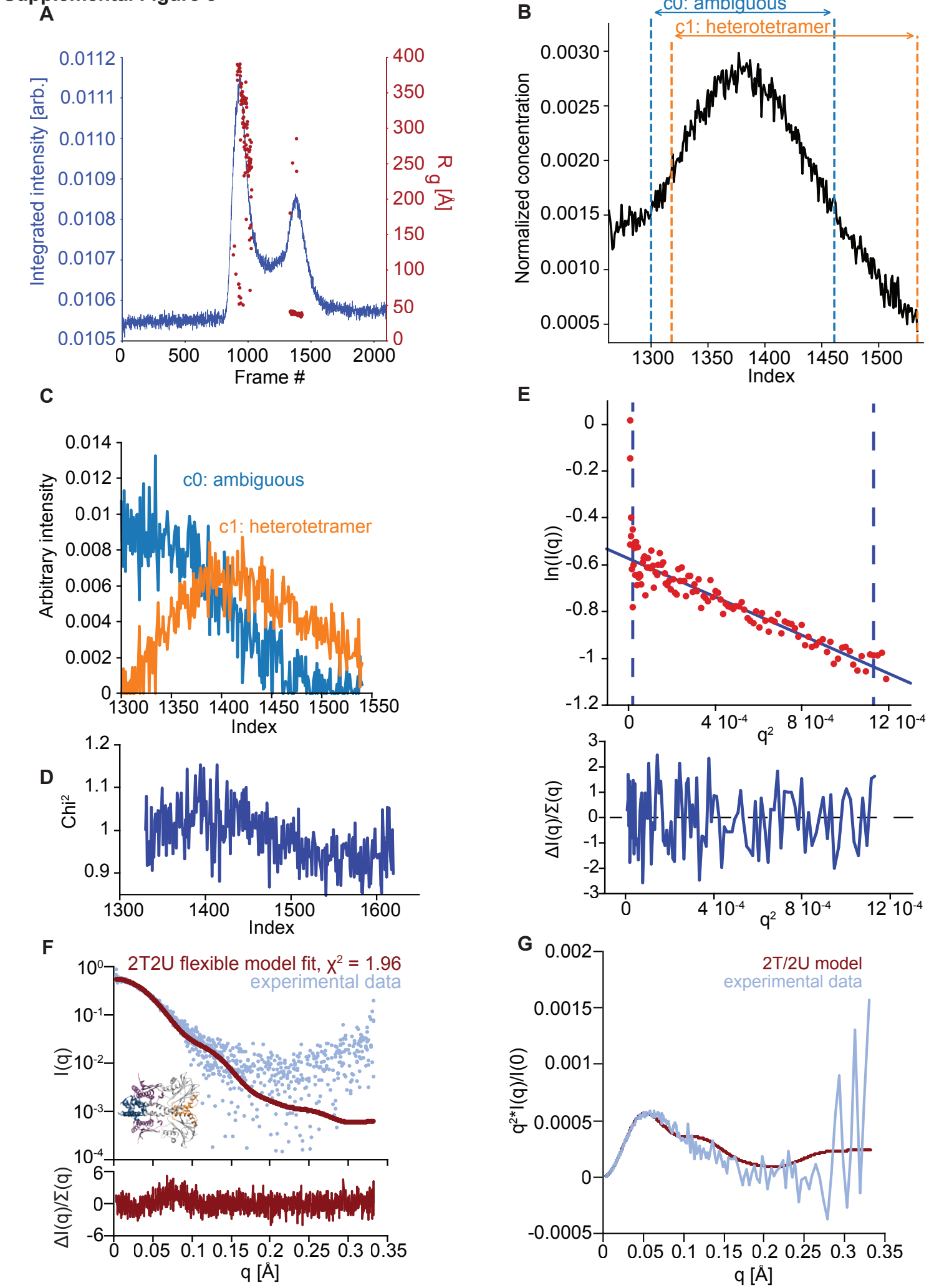

Supplemental Figure 5: EFA deconvolution and Guinier analysis of RsbT/RsbUQ94L SAXS profiles

A SAXS data summary for RsbT/RsbU^{Q94L}. Series intensity (blue, left axis) versus frames, and R_g versus frame (red, right axis) are plotted. **B** The selected intensity range for EFA (black) (frame index 1300-1540), and the individual component ranges for deconvolution; blue denotes the range of frames where the scattering component we assigned as c0, ambiguous component, was detected (1300-1461) and orange denotes the range of frames where the scattering component we assigned as c1, the 2RsbT/2RsbU^{Q94L} heterotetrametric complex, was detected (1318-1540). **C** Area normalized concentration profiles for 2RsbT/2RsbU^{Q94L} heterotetrameric complex (orange) and ambiguous component (blue). **D** Mean χ2 values for the EFA deconvolution fit to the original scattering data. **E** Guinier fit for 2RsbT/2RsbU^{Q94L} heterotetrameric complex component on the upper plot and uncertainty normalized residuals of the fit on the lower plot. The scattering data for the dimer component (red) is fit to the Guinier approximation (blue). The blue dashed lines are the q_{min} and q_{max} at values 0.0033 Å-1 and 0.0336 Å-1, respectively. **F** I(q) versus q plot of the heterotetrameric complex component of SAXS scattering data from 2RsbT/2RsbU (blue) overlaid with a MultiFoXS generated two-state profile fit with flexibility allowed for residues 82-96 (red). The upper plot shows I(q) versus q on the log-linear axes while the lower plot shows the uncertainty normalized residuals of the fit ((experimental-computed)/error), χ^2 of 1.96. The one-state flexible model is shown with a RMSD to the AlphaFold2 prediction of 2RsbT/2RsbU (1.36Å). **G** Kratky plot of SAXS scattering data from the heterotetrameric component of 2RsbT/2RsbU experimental data (blue) overlaid with the profile computed by FoXS based on the AlphaFold2 model of an RsbT/RsbU heterotetramer (red). The experimental profile was logarthmically binned to reduce noise at high q.

Supplemental Figure 6

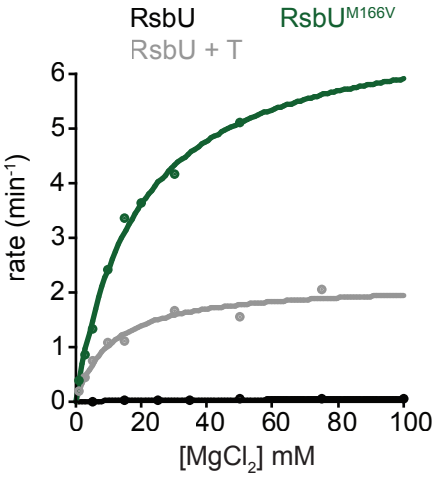

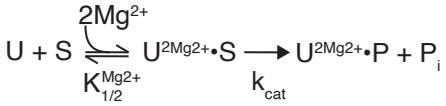

85(11) mM 0.088(2.2) min⁻¹

19 mM 7.03 min⁻¹

Supplemental Figure 6: RsbU is activated through a conserved switch element

The rate of dephosphorylation of RsbV-P is plotted as a function of concentration of $MgCl_2$. The observed rates for $RsbU^{M166V}$ (green) and wild-type RsbU in the presence (black) and absence of RsbT (grey) are shown. The curves are fits to the Michaelis-Menten equation using non-linear curve fitting. The k_{cat} of wild-type RsbU is 2.2 ± 0.16 min^{-1} with RsbT and 0.088 ± 0.023 min^{-1} without RsbT, and the k_{cat} of $RsbU^{Q94L}$ is 7.03 ± 0.35 min^{-1} without RsbT. The K_M^{MgCl2} of wild-type RsbU is 11 ± 2.6 mM with RsbT and 85 ± 38 mM without RsbT, and the K_M^{MgCl2} of $RsbU^{M166V}$ is 19 ± 2.1 mM. The lower panel is a summary of a reaction scheme of RsbU dephosphorylating RsbV-P (denoted as S) with Mg^{2+} cofactor, with the K_M^{MgCl2} and k_{cat} calculated values below. Errors are the error of the fit.

Supplemental Figure 7

A *M. tubercolisis* Rv1364c

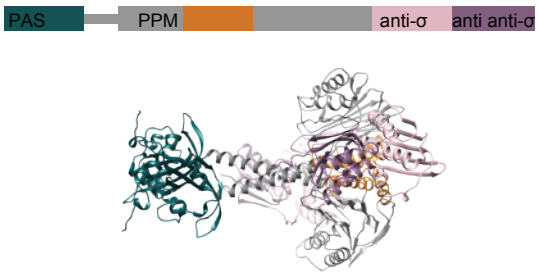

B *S. coelicolor* OsaC

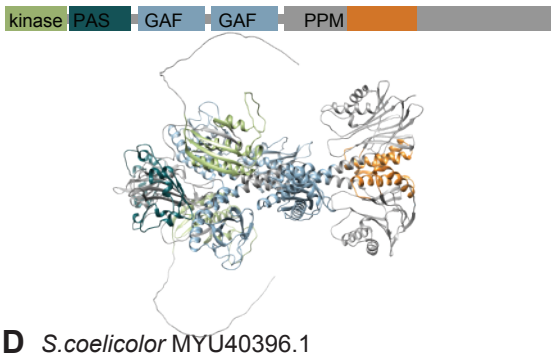

C *R. aetherivorans* WP_029544106.1

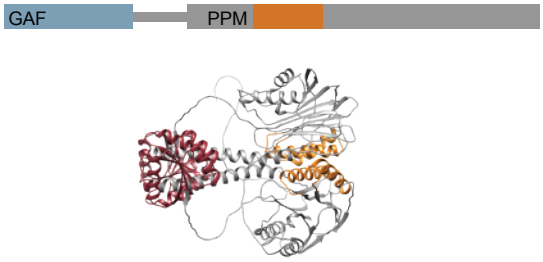

D *S.coelicolor* MYU40396.1

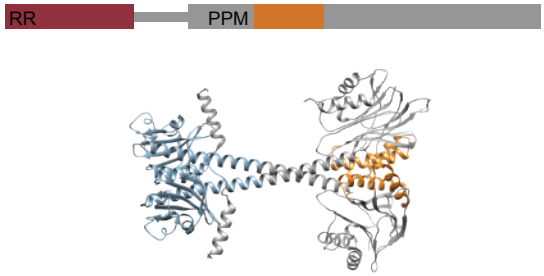

E *Synechocystis sp.* WP_010874143.1

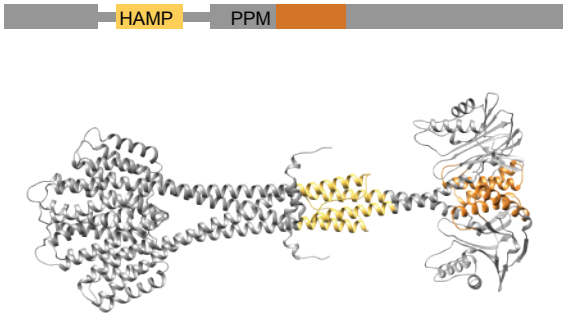

Supplemental Figure 7: AlphaFold2 predictions of varying signaling PPM phosphatases

A An AlphaFold2 model of the *M. tubercolisis* GSR phosphatase Rv1364c is shown with a N-terminal PAS domain colored turquoise that connects to the PPM phosphatase domain colored grey, an anti-σ domain (related to RsbW) colored pink and an anti-anti-σ domain (related to RsbV) colored purple. The switch element of the PPM phosphatase domain (α1 and α2) is colored orange. **B** An AlphaFold2 model of the *S. coelicolor* OsaC GSR phosphatase is shown with a N-terminal RsbW-like kinase domain colored in green, connected to a PAS domain colored in turquoise, tandem GAF domains colored in blue, and a PPM phosphatase colored in grey. The switch element of the PPM phosphatase domain (α1 and α2) is colored orange. **C** An AlphaFold2 model of a dimer of the phosphatase from *S. coelicolor* (WP_011031544.1) is shown with the PAS domain colored in turquoise connected to the PPM phosphatase colored in grey. The switch element of the PPM phosphatase domain (α1 and α2) is colored orange. **D** An AlphaFold2 model of a dimer of the phosphatase from *R. aetherivorans* (WP_029544106.1) is shown with the GAF domain colored in blue connected to the PPM phosphatase colored in grey. The switch element of the PPM phosphatase domain (α1 and α2) is colored orange. **E** An AlphaFold2 model of a dimer of the phosphatase from *S. coelicolor* (MYU40396.1) is shown with the response receiver domain colored in red connected to the PPM phosphatase colored in grey. The switch element of the PPM phosphatase domain (α1 and α2) is colored orange. **F** An AlphaFold2 model of a dimer of the phosphatase from *Synechocystis* species (WP_010874143.1) is shown with the HAMP domain colored in yellow connected to the PPM phosphatase colored in grey. The switch element of the PPM phosphatase domain (α1 and α2) is colored orange. The structure models in all panels are shown aligned by the top PPM domain to highlight the conservation of the PPM dimer in predictions of dimeric phosphatases with diverse regulatory domains.

Supplemental Figure 8

B. subtilis RsbU

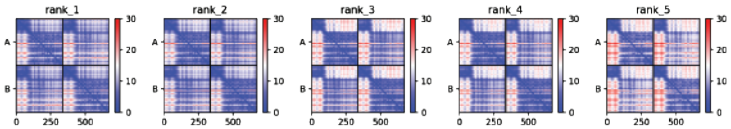

B. subtilis RsbT RsbU

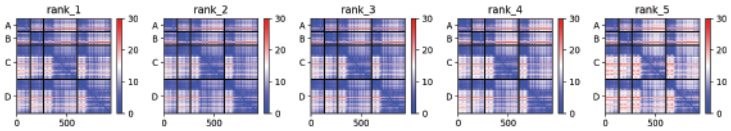

B. subtilis RsbP RsbQ

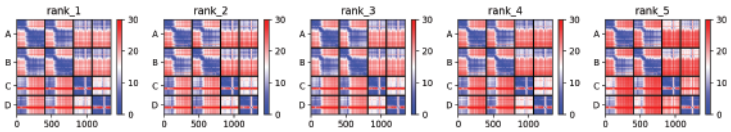

C. difficile RsbZ

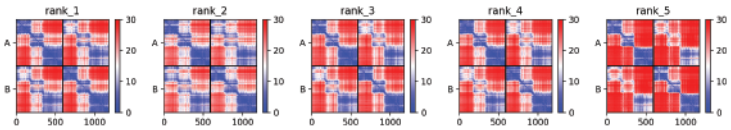

Gammaproteobacteria sp. NreB

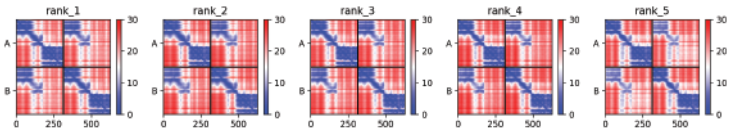

M. thermoacetica MtG

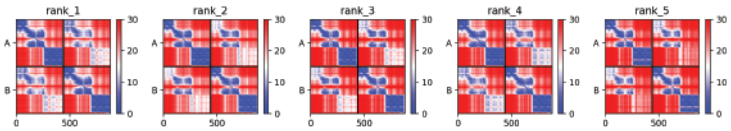

M. tubercolisis Rv1364c

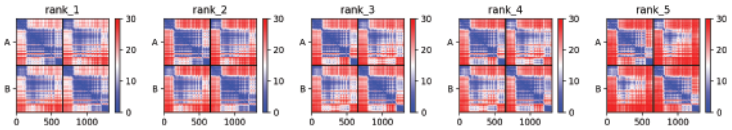

S. coelicolor OsaC

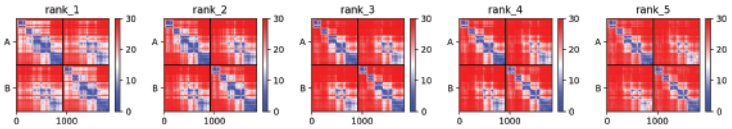

R. aetherivorans WP_029544106.1

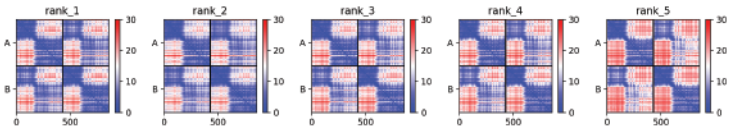

S. coelicolor MYU40396.1

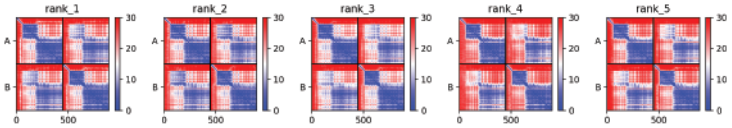

Synechocystis sp. WP_010874143.1

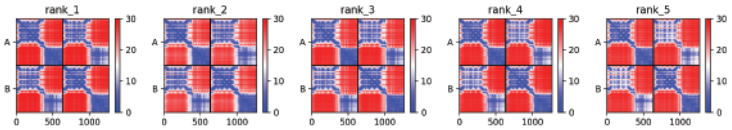

Supplemental Figure 8: PAE plots of AlphaFold2 prediction

Predicted aligned error of the AlphaFold2 structure predictions of the following proteins: *B. subtilis* RsbU, *B. subtilis* RsbT/RsbU complex, *B. subtilis* RsbP/RsbQ complex, *C. difficile* RsbZ, *Gammaproteobacteria* sp. NreB, *M. thermoacetica* MtG, *M. tuberculosis* Rv1364c, *S. coelicolor* OsaC, *S. coelicolor* WP_011031544.1, *R. aetherivorans* WP_029544106.1, *S. coelicolor* MYU40396.1, and *Synechocystis* sp. WP_010874143.1.

Table 1

(*a*) Sample details		
	RsbU	$RsbU^{Q94L}$/RsbT
Organism	*B. subtilis*	*B. subtilis*
Description:	RsbU (1-335) Uniprot ID: P40399 GPG scar from 6His cleavage	$RsbU^{Q94L}$ (1-335) Uniprot ID: P40399; RsbT (1-133) Uniprot ID: P42411, 6His with 3C cleavage site
Extinction coefficient ε (280nm)	26,820 $M^{-1}cm^{-1}$	$RsbU^{Q94L}$: 26,820 $M^{-1}cm^{-1}$ RsbT: 13,980 $M^{-1}cm^{-1}$
Molecular mass *M* from chemical composition	38.6 kDa	RsbT: 14.3 kDa $RsbU^{Q94L}$: 38.6 kDa
For SEC-SAX, loading volume/concentration	3.5 mg ml^{-1}	2.5 mg ml^{-1}
injection volume, flow rate	300µl, 0.6 ml min^{-1}	300µl, 0.6 ml min^{-1}
Solvent composition and source	20 mM HEPES pH 7.5, 100 mM NaCl, 5 mM DTT	20 mM HEPES pH 7.5, 100 mM NaCl, 5 mM DTT
(*b*) SAX data collection parameters		
Source, instrument and description	BioCAT facility at the Advanced Photon Source beamline 18ID with Pilatus3 X 1M (Dectris) detector	
Wavelength	1.033 Å	
Beam size (μm^2)	150 (h) x 25 (v) focused at the detector	
Camera length	3.682 m	
q-measurement range	0.0027-0.33 $Å^{-1}$	
Absolute scaling method	Glassy Carbon, NIST SRM 3600	
Basis for normalization to constant counts	To transmitted intensity by beam-stop counter	
Method for monitoring radiation damage	Automated frame-by-frame comparison of relevant regions using CORMAP algorithm (Franke *et al.*, 2015) implemented in BioXTAS RAW	
Exposure time	0.5 s exposure time with a 1 s total exposure period (0.5 s on, 1.5 s off) of entire SEC elution	
Sample configuration	SEC-MALS-SAXS. Size separation used a Superdex 200 10/300 Increase GL column and a 1260 Infinity II HPLC (Agilent Technologies). UV data was measured in the Agilent, and MALS-DLS-RI data by DAWN HELEOS-II (17 MALS + 1 DLS channels) and Optilab T-rEX (RI) instruments (Wyatt Technology). SAXS data was measured in a sheath-flow cell (Kirby et al., 2016), effective path length 0.542mm.	
Sample temperature	22 ºC	
(*c*) Software employed for SAXS data reduction, analysis and interpretation		
MALS-DLS-RI analysis	Astra 7 (Wyatt)	
SAX data reduction	Radial averaging; frame comparison, averaging, and subtraction done using BioXTAS RAW 2.1.4 (Hopkins *et al*., 2017). Deconvolution of overlapping peaks by EFA (Meisburger *et al*., 2016) as implemented in RAW.	
Basic analyses:	Guinier fit and molecular weight using BioXTAS RAW 2.1.4, P(r) function using GNOM (Svergun, 1992). RAW uses MoW and Vc molecular weight methods (Rambo & Tainer, 2013; Piiadov *et al*., 2018) ATSAS Version 3.2.1 (Manalastas-Cantos et al. 2021).	

FoXS	Calculated predicted scattering profiles from the model (FoXS) (Schneidman-Duhovny *et al*., 2013; Schneidman-Duhovny *et al*., 2016)	
MultiFoxS	Calculated predicted scattering profiles from the multicomponent fits from a generated flexible structure ensemble (MultiFoXS) (Schneidman-Duhovny *et al*., 2016)	
(*d*) Structural parameters		
Figure 4 components	c0: RsbU dimer	c1: 2T/2U^{Q94L} heterotetramer
Guinier Analysis		
I(0) (Arb.)	5.632 ± 0.008	0.564 ± 0.003
R_g	39.05 ± 0.16 Å	35.06 ± 0.43 Å
q-range	0.0036 - 0.0234 Å^{-1}	0.0033 – 0.0336 Å^{-1}
$q_{max}R_g$	0.916	1.178
Coefficient of correlation, r^2	0.995	0.88
Volume (adjusted V_P as SAXS MoW2)	116000 Å^3	124000 Å^3
MW, MoW2 method (ratio to expected)	96.2 kDa (1.25)	103.2 kDa (0.98)
MW, Vc method (kDa) (ratio to expected)	75.6 kDa (0.98)	83.9 kDa (0.80)
P(*r*) analysis		
I(0) (Arb.)	5.648 ± 0.007	0.561 ± 0.003
R_g	39.98 ± 0.12 Å	34.87 ± 0.36 Å
D_{max}	168 Å	176 Å
q-range	0.0035 - 0.3327 Å^{-1}	0.005 – 0.3327 Å^{-1}
χ^2 (total estimate from GNOM)	1.257 (0.729)	1.374 (0.691)
FoXS		
R_g	34.05 Å	33.68 Å
χ^2	12.53	1.83
c_1	1.02	1.04
c_2	1.91	-1.77
MultiFoXS		
# of conformations	10,000	10,000
flexible residues	82 - 96	82 – 96
# of states	2	1
R_g	34.91 Å (71%) 45.69 Å (29%)	33.28 Å
χ^2	1.2	1.96
c_1	1.0	0.99
c_2	3.91	-0.5
Additional EFA components	c1: truncated dimer	c0: ambiguous
Guinier Analysis		
I(0) (Arb.)	1.042 ± 0.004	0.478 ± 0.003
R_g	28.14 ± 0.17 Å	42.18 ± 0.48 Å
q-range	0.0027 - 0.0461 Å^{-1}	0.005 – 0.0305 Å^{-1}
$q_{max}R_g$	1.298	1.295
Coefficient of correlation, r^2	0.931	0.948
Volume (adjusted V_P as SAXS MoW2)	64500 Å^3	197000 Å^3

MW, MoW2 method (ratio to expected)	53.6 kDa	163.5 kDa (1.55)
MW, Vc method (kDa) (ratio to expected)	48.8 kDa	145.3 kDa (1.37)
P(*r*) analysis		
I(0) (Arb.)	1.055 ± 0.004	0.486 ± 0.004
R_g	29.29 ± 0.13 Å	45.18 ± 0.48 Å
D_{max}	98.0 Å	124 Å
q-range	0.0027 - 0.3327 $Å^{-1}$	0.0027 – 0.3327 $Å^{-1}$
χ^2 (total estimate from GNOM)	1.421 (0.924)	1.628 (0.84)

Supplementary Table S1:

***B. subtilis* Strains (all *B. subtilis* strains are in the background of PY79)**

Strain #	Genotype	Reference
RB01	Δ*rsbPQ* Δ*rsbU rsbV-FLAG amyE::ctc-lacZ Pspank-rsbU*	Ho, K. & Bradshaw, N., 2021
RB02	Δ*rsbPQ* Δ*rsbTU rsbV-FLAG amyE::ctc-lacZ Pspank-rsbU*	Ho, K. & Bradshaw, N., 2021
RB03	Δ*rsbPQ* Δ*rsbTU rsbV-FLAG amyE::ctc-lacZ Pspank-rsbTU*	Ho, K. & Bradshaw, N., 2021
RB04	Δ*rsbPQ* Δ*rsbU rsbV-FLAG amyE::ctc-lacZ Pspank-rsbU*^{Q94L}	This study
RB05	Δ*rsbPQ* Δ*rsbTU rsbV-FLAG amyE::ctc-lacZ Pspank-rsbU*^{Q94L}	This study
RB06	Δ*rsbPQ* Δ*rsbU rsbV-FLAG amyE::ctc-lacZ Pspank-rsbU*^{M166V}	Ho, K. & Bradshaw, N., 2021
RB07	Δ*rsbPQ* Δ*rsbTU rsbV-FLAG amyE::ctc-lacZ Pspank-rsbU*^{M166V}	Ho, K. & Bradshaw, N., 2021
RB08	Δ*rsbPQ* Δ*rsbTU rsbV-FLAG amyE::ctc-lacZ Pspank-rsbTU*^{Y28I}	This study
RB09	Δ*rsbPQ* Δ*rsbTU rsbV-FLAG amyE::ctc-lacZ Pspank-rsbTU*^{Y28I,S49G}	This study
RB10	Δ*rsbPQ* Δ*rsbTU rsbV-FLAG amyE::ctc-lacZ Pspank-rsbTU*^{Y28I,K53E}	This study
RB11	Δ*rsbPQ* Δ*rsbTU rsbV-FLAG amyE::ctc-lacZ Pspank-rsbTU*^{Y28I,T89A}	This study
RB12	Δ*rsbPQ* Δ*rsbTU rsbV-FLAG amyE::ctc-lacZ Pspank-rsbTU*^{Y28I,G92R}	This study
RB13	Δ*rsbPQ* Δ*rsbTU rsbV-FLAG amyE::ctc-lacZ Pspank-rsbTU*^{Y28I,G92E}	This study
RB14	Δ*rsbPQ* Δ*rsbTU rsbV-FLAG amyE::ctc-lacZ Pspank-rsbTU*^{Y28I,Q94L}	This study
RB15	Δ*rsbPQ* Δ*rsbTU rsbV-FLAG amyE::ctc-lacZ Pspank-rsbTU*^{Y28I,T110S}	This study
RB16	Δ*rsbPQ* Δ*rsbTU rsbV-FLAG amyE::ctc-lacZ Pspank-rsbTU*^{Y28I,V142A}	This study
RB17	Δ*rsbPQ* Δ*rsbTU rsbV-FLAG amyE::ctc-lacZ Pspank-rsbTU*^{Y28I,K143E}	This study
RB18	Δ*rsbPQ* Δ*rsbTU rsbV-FLAG amyE::ctc-lacZ Pspank-rsbTU*^{Y28I,C165Y}	This study
RB19	Δ*rsbPQ* Δ*rsbTU rsbV-FLAG amyE::ctc-lacZ Pspank-rsbTU*^{Y28I,M173I}	This study
RB20	Δ*rsbPQ* Δ*rsbTU rsbV-FLAG amyE::ctc-lacZ Pspank-rsbTU*^{R91E}	This study
RB21	Δ*rsbPQ* Δ*rsbTU rsbV-FLAG amyE::ctc-lacZ Pspank-rsbT*^{D92K}*U*	This study
RB22	Δ*rsbPQ* Δ*rsbTU rsbV-FLAG amyE::ctc-lacZ Pspank-rsbT*^{D92K}*U*^{R91E}	This study
RB23	Δ*rsbPQ* Δ*rsbU rsbV-FLAG amyE::ctc-lacZ Pspank-rsbU*^{Q94I}	This study
RB24	Δ*rsbPQ* Δ*rsbTU rsbV-FLAG amyE::ctc-lacZ Pspank-rsbU*^{Q94I}	This study
RB25	Δ*rsbPQ* Δ*rsbU rsbV-FLAG amyE::ctc-lacZ Pspank-rsbU*^{Q94V}	This study
RB26	Δ*rsbPQ* Δ*rsbTU rsbV-FLAG amyE::ctc-lacZ Pspank-rsbU*^{Q94V}	This study
RB27	Δ*rsbPQ* Δ*rsbU rsbV-FLAG amyE::ctc-lacZ Pspank-rsbU*^{Q94Y}	This study
RB28	Δ*rsbPQ* Δ*rsbTU rsbV-FLAG amyE::ctc-lacZ Pspank-rsbU*^{Q94Y}	This study
RB29	Δ*rsbPQ* Δ*rsbU rsbV-FLAG amyE::ctc-lacZ Pspank-rsbU*^{Q94F}	This study
RB30	Δ*rsbPQ* Δ*rsbTU rsbV-FLAG amyE::ctc-lacZ Pspank-rsbU*^{Q94F}	This study
RB31	Δ*rsbPQ* Δ*rsbU rsbV-FLAG amyE::ctc-lacZ Pspank-rsbU*^{Q94W}	This study

RB32	Δ*rsbPQ* Δ*rsbTU rsbV-FLAG amyE::ctc-lacZ Pspank-rsbU*^{Q94W}	This study
RB33	Δ*rsbPQ* Δ*rsbU rsbV-FLAG amyE::ctc-lacZ Pspank-rsbU*^{Q94M}	This study
RB34	Δ*rsbPQ* Δ*rsbTU rsbV-FLAG amyE::ctc-lacZ Pspank-rsbU*^{Q94M}	This study
RB35	Δ*rsbPQ* Δ*rsbU rsbV-FLAG amyE::ctc-lacZ Pspank-rsbU*^{Q94N}	This study
RB36	Δ*rsbPQ* Δ*rsbTU rsbV-FLAG amyE::ctc-lacZ Pspank-rsbU*^{Q94N}	This study
RB37	Δ*rsbPQ* Δ*rsbU rsbV-FLAG amyE::ctc-lacZ Pspank-rsbU*^{Q94E}	This study
RB38	Δ*rsbPQ* Δ*rsbTU rsbV-FLAG amyE::ctc-lacZ Pspank-rsbU*^{Q94E}	This study
RB39	Δ*rsbPQ* Δ*rsbU rsbV-FLAG amyE::ctc-lacZ Pspank-rsbU*^{Q94A}	This study
RB40	Δ*rsbPQ* Δ*rsbTU rsbV-FLAG amyE::ctc-lacZ Pspank-rsbU*^{Q94A}	This study
RB41	Δ*rsbPQ* Δ*rsbU rsbV-FLAG amyE::ctc-lacZ Pspank-rsbU*^{Q94G}	This study
RB42	Δ*rsbPQ* Δ*rsbTU rsbV-FLAG amyE::ctc-lacZ Pspank-rsbU*^{Q94G}	This study
RB43	Δ*rsbPQ* Δ*rsbU rsbV-FLAG amyE::ctc-lacZ Pspank-rsbU*^{T89A}	This study
RB44	Δ*rsbPQ* Δ*rsbU rsbV-FLAG amyE::ctc-lacZ Pspank-rsbU*^{C165Y}	This study

Supplementary Table S2:

***E. coli* Strains**

Strain #	Genotype	Reference
RB45	*BL21 (DE3) pET47b 6H-3C-rsbT*	Ho, K. & Bradshaw, N., 2021
RB46	*BL21 (DE3) pET47b 6H-3C-rsbU*	Ho, K. & Bradshaw, N., 2021
RB47	*BL21 (DE3) pET47b 6H-3C-rsbV*	Ho, K. & Bradshaw, N., 2021
RB48	*BL21 (DE3) pET47b 6H-3C-rsbW*	Ho, K. & Bradshaw, N., 2021
RB49	*BL21 (DE3) pET47b 6H-3C-rsbVW*	This study
RB50	*BL21 (DE3) pET47b 6H-3C-rsbU*^{Q94L}	This study
RB51	*BL21 (DE3) pET47b 6H-3C-rsbU*^{M166V}	Ho, K. & Bradshaw, N., 2021
RB52	*BL21 (DE3) pET47b 6H-3C-rsbTU*	This study
RB53	*BL21 (DE3) pET47b 6H-3C-rsbU*^{R91E}	This study
RB54	*BL21 (DE3) pET47b 6H-3C-rsbTU*^{Q94L}	This study
RB55	*DH5 α Pspank-rsbU*	Ho, K. & Bradshaw, N., 2021
RB56	*DH5 α Pspank-rsbTU*	Ho, K. & Bradshaw, N., 2021
RB57	*DH5 α rsbU*^{Q94L}	
RB58	*DH5 α Pspank-rsbU*^{M166V}	Ho, K. & Bradshaw, N., 2021
RB59	*DH5 α Pspank-rsbTU*^{Y28I}	This study
RB60	*DH5 α Pspank-rsbTU*^{Y28I,S49G}	This study
RB61	*DH5 α Pspank-rsbTU*^{Y28I,K53E}	This study
RB62	*DH5 α Pspank-rsbTU*^{Y28I,T89A}	This study
RB63	*DH5 α Pspank-rsbTU*^{Y28I,G92R}	This study
RB64	*DH5 α Pspank-rsbTU*^{Y28I,G92E}	This study
RB65	*DH5 α Pspank-rsbTU*^{Y28I,Q94L}	This study
RB66	*DH5 α Pspank-rsbTU*^{Y28I,T110S}	This study
RB67	*DH5 α Pspank-rsbTU*^{Y28I,V142A}	This study
RB68	*DH5 α Pspank-rsbTU*^{Y28I,K143E}	This study
RB69	*DH5 α Pspank-rsbTU*^{Y28I,C165Y}	This study
RB70	*DH5 α Pspank-rsbTU*^{Y28I,M173I}	This study
RB71	*DH5 α Pspank-rsbTU*^{R91E}	This study

RB72	*DH5 α Pspank-rsbT^{D92K}U*	This study
RB73	*DH5 α Pspank-rsbT^{D92K}U^{R91E}*	This study
RB74	*DH5 α Pspank-rsbU^{Q94I}*	This study
RB75	*DH5 α Pspank-rsbU^{Q94V}*	This study
RB76	*DH5 α Pspank-rsbU^{Q94Y}*	This study
RB77	*DH5 α Pspank-rsbU^{Q94Y}*	This study
RB78	*DH5 α Pspank-rsbU^{Q94F}*	This study
RB79	*DH5 α Pspank-rsbU^{Q94W}*	This study
RB80	*DH5 α Pspank-rsbU^{Q94M}*	This study
RB81	*DH5 α Pspank-rsbU^{Q94N}*	This study
RB82	*DH5 α Pspank-rsbU^{Q94E}*	This study
RB83	*DH5 α Pspank-rsbU^{Q94A}*	This study
RB84	*DH5 α Pspank-rsbU^{Q94G}*	This study
RB85	*DH5 α Pspank-rsbU^{T89A}*	This study
RB86	*DH5 α Pspank-rsbU^{C165Y}*	This study